Journal of Materials Research and Technology 42 (2026) 8726–8747

Contents lists available at ScienceDirect

Journal of Materials Research and Technology

journal homepage: www.elsevier.com/locate/jmrt

A grand-potential phase-field approach for modeling pitting corrosion and pressure-driven cracking in multiphase alloys

Akash Kumar [a,c,*], Nishant Prajapati [a], Martin Reder [b,c], Ravi Kumar Jeela [b], Daniel Schneider [a,b,c], Britta Nestler [a,b,c]

[a] Institute of Nanotechnology (INT), Karlsruhe Institute of Technology (KIT), Hermann-von-Helmholtz-Platz 1, Eggenstein-Leopoldshafen, 76344, Germany
[b] Institute for Digital Materials Science (IDM), Karlsruhe University of Applied Sciences, Moltkestraße 30, Karlsruhe, 76133, Germany
[c] Institute for Applied Materials - Microstructure Modelling and Simulation (IAM-MMS), Karlsruhe Institute of Technology (KIT), Straße am Forum 7, Karlsruhe, 76131, Germany

ARTICLE INFO

Dataset link: Pace3D

Keywords:
Corrosion
Pressure-induced crack
Grand potential approach
Phase-field modeling

ABSTRACT

This work introduces a phase-field model based on the grand potential formulation for simulating corrosion in multiphase systems, validated against analytical solutions and numerical benchmarks. The framework investigates corrosion processes in complex microstructures, emphasizing how interfacial mobility governs pit evolution. In order to simulate fluid-pressure induced crack growth in these corrosion pits, the phase-field fracture model for brittle materials was extended to account for application of pressure along the pit surface. The results show that increasing pit depth in multiphase systems significantly reduces the critical relative pressure required for crack initiation and propagation, demonstrating the strong linkage between morphology and mechanical failure within the present comparative phase-field framework. These dynamics are analyzed across multiple microstructural configurations, illustrating how phase boundaries and local topology influence degradation through pitting and subsequent micro-crack formation. This work advances mesoscale corrosion–mechanics understanding by (1) integrating grand potential–driven dissolution with pressure-dependent fracture analysis in a sequential morphology-to-failure framework and (2) clarifying how variations in interfacial mobility within multiphase alloys control pit development and the susceptibility to pressure-induced cracking. The findings provide insights relevant to structural components such as piping systems and flow channels in industrial environments where corrosion and internal pressure coexist.

1. Introduction

Localized corrosion, particularly pitting, is a critical degradation mechanism in structural alloys exposed to aggressive environments. Unlike uniform dissolution, pitting produces highly irregular morphologies that act as stress concentrators, promoting crack initiation and ultimately governing the mechanical reliability and service life of engineering components [1–3]. The progression from pit formation to crack nucleation has been widely documented across stainless steels, aluminum alloys, and high-strength steels [4,5], highlighting the need for mechanistic models capable of capturing both the evolution of pit morphology and its role in promoting localized mechanical failure.

Pitting corrosion is particularly severe in environments containing hot, chloride-rich brines, such as those encountered in geothermal systems, marine structures, and chemical processing facilities [6,7]. In such conditions, elevated temperatures, high ionic strength, and dissolved species including Cl^-, CO_2, and H_2S destabilize protective films on metallic surfaces and promote localized dissolution [8,9]. These chemistries frequently lead to rapid pit development and subsequent cracking in steels and corrosion-resistant alloys, underscoring the importance of predictive tools that can relate microstructural features to pit morphology and the onset of mechanically assisted failure.

Pitting corrosion is particularly critical in high-strength alloys such as stainless steels and aluminum alloys, where breakdown of the passive film leads to highly localized dissolution and the formation of deep, sharp cavities [2,4]. These pits act as strong stress concentrators and frequently serve as sites for crack initiation, thereby governing the mechanical reliability and service life of engineering components [3,5]. Experimental and field studies have documented rapid pit growth and pit-to-crack transitions under aggressive chemistries, demonstrating that susceptibility to pit-induced cracking depends strongly on local

---

* Corresponding author at: Institute for Applied Materials - Microstructure Modelling and Simulation (IAM-MMS), Karlsruhe Institute of Technology (KIT), Straße am Forum 7, Karlsruhe, 76131, Germany.

E-mail address: akash.kumar@kit.edu (A. Kumar).

https://doi.org/10.1016/j.jmrt.2026.05.130
Received 29 January 2026; Accepted 11 May 2026

Available online 15 May 2026
2238-7854/© 2026 The Authors. Published by Elsevier B.V. This is an open access article under the CC BY license (http://creativecommons.org/licenses/by/4.0/).

environment, alloy composition, and microstructure [10,11]. In particular, chloride-containing brines, dissolved gases, and elevated temperatures promote accelerated pit deepening and subsequent cracking in both carbon steels and corrosion-resistant alloys. Although advanced materials such as duplex and high-nickel stainless steels exhibit improved resistance to localized corrosion, deep pits and pit-induced fracture are still frequently observed under severe conditions [12–14]. These observations underscore the need for predictive, microstructure-sensitive mechanistic models capable of resolving pit morphology evolution and assessing the conditions under which localized corrosion triggers mechanical failure.

Numerical models for pitting corrosion have traditionally relied on sharp-interface formulations that track the moving metal–electrolyte boundary through prescribed interface kinetics or electrochemical boundary conditions [15–18]. Although these methods can capture dissolution processes, they often require explicit interface tracking, remeshing, or level-set reconstruction to represent evolving pit geometries [19–21]. Such approaches become increasingly cumbersome in concentrated electrolytes, where dissolution is governed by chemical potential gradients [22], or when pits interact with microstructural features. Alternative frameworks, including ALE methods, mesh-free schemes such as peridynamics, and cellular automata models, offer various advantages but still face challenges when simulating complex interfaces or assessing pit-induced mechanical response [23–25]. These limitations have motivated the use of phase-field methods, which naturally accommodate evolving morphologies without explicit interface tracking.

The phase-field method provides a flexible alternative for modeling dissolution processes, as it represents the metal–electrolyte interface through a diffuse order parameter and eliminates the need for explicit interface tracking [26]. Early phase-field corrosion models primarily focused on electrochemical formulations, linking interface kinetics to local current density (using Butler–Volmer/Tafel kinetics approach) or pH-dependent reaction rates [27,28]. Subsequent studies incorporated film precipitation, galvanic effects, or microstructural features to explore complex pit morphologies and electrochemically assisted cracking [29–32]. While these frameworks have advanced understanding of localized corrosion, most rely on conventional Ginzburg–Landau [29] or Kim–Kim–Suzuki formulations [27] and face challenges when applied to multiphase alloys or when assessing pit-induced mechanical failure under evolving geometries.

Despite these advances, existing phase-field corrosion models remain limited in their ability to handle multiphase alloys and to evaluate pit-induced mechanical failure in evolving geometries. Most formulations are based on traditional free-energy descriptions that tightly couple interface width and energy, making it difficult to represent complex microstructures or to efficiently simulate dissolution in multi-component systems. In contrast, the grand-potential phase-field framework [33] decouples these quantities, enables straightforward control of interfacial properties, and has demonstrated scalability in other multi-phase, multi-component problems; in this work, it is implemented within the Pace3D simulation framework [34], a multiphysics platform designed to model complex microstructure evolution under coupled physical influences, whose integrated data analysis capabilities facilitate the identification of pore–structure–property relationships and provide deep insight into the underlying physical mechanisms. Yet, this formulation has not been applied to corrosion, leaving a significant gap in modeling corrosion-driven degradation in heterogeneous alloys where interface energetics and microstructure strongly influence pit evolution. The modeling approach adapted in this work is intended to capture the mechanistic evolution of pit morphology and its influence on pressure-induced cracking, rather than to predict absolute corrosion rates or fully coupled chemo-mechanical interactions.

In this study, we address these gaps by adopting a grand-potential-based phase-field model to simulate pitting corrosion, alongside a phase-field fracture model to capture the subsequent mechanical failure driven by pressure-induced cracking in metallic alloys under conditions representative of the interior environments of pipelines and channels in geothermal systems. Given the significantly different timescales typically associated with pitting corrosion and crack formation, the two processes are simulated here in a decoupled manner. This treatment is intended to isolate the mechanistic role of corrosion-pit morphology in pressure-induced crack initiation while reducing modeling complexity. In practice, it also offers computational advantages relative to a fully coupled treatment, although a formal performance benchmark is beyond the scope of the present work. It is most appropriate for regimes in which pit evolution is much slower than the quasi-static mechanical response and in which feedback from local stress states to dissolution kinetics remains of secondary importance. To model pressure-induced cracking, pressure is applied at the fluid–metal surface using a diffuse-interface approach by extending the mechanical model with a whole-domain formulation of the linear momentum balance. The phase-field modeling framework is validated through benchmark tests in pseudo-1D and 2D systems and is subsequently applied to study how cracks nucleate and propagate under increasing pressure at the fluid-metals surface with corrosion pits. We further extend the analysis to dual-phase and multi-phase alloy microstructures, examining how metallic phase arrangements influence pit morphology evolution and susceptibility to cracking. The article is organized as follows: Section 2 presents the phase-field model equations for simulating corrosion and crack formation. Section 3 details the simulation results and provides a systematic discussion. Finally, Section 4 concludes the article and outlines potential directions for future research.

2. Methods

This section presents the grand-potential phase-field formulation used to simulate dissolution-driven pit evolution in multiphase alloys and the subsequent phase-field fracture model employed to simulate pressure-induced cracking. Because corrosion and crack formation evolve on markedly different time scales, the two processes are treated sequentially. This sequential treatment is intended for regimes in which pit morphology evolves over a much longer timescale than the quasi-static mechanical response, so that the dominant effect of corrosion on fracture is the geometric weakening introduced by the pit. Corrosion simulations first yield the pit morphology and surface geometry, which are then used as inputs to the fracture mechanics problem. Pressure loading is applied through a diffuse-interface representation of the fluid–solid boundary, and fracture evolution is computed using the phase-field fracture formulation of brittle materials. This sequential framework isolates the mechanistic influence of pit morphology on crack initiation and enables systematic evaluation of microstructure-dependent failure susceptibility. The governing equations for the corrosion and fracture models, along with the numerical implementation, are presented in the following subsections.

2.1. Multiphase field model based on grand-potential approach

2.1.1. Multiphase and multicomponent system

A multiphase-field model is used to simulate corrosion in metallic pipes. This model is derived from a grand potential functional, following the formulation of Choudhury et al. [33]. The grand potential functional Ω (in J) depends on the order parameters $\boldsymbol{\phi} = \{\phi_\alpha, \ldots, \phi_N\}$ (dimensionless) of N phases and the volumetric chemical potentials $\boldsymbol{\mu} = \{\mu_1, \mu_2, \ldots, \mu_{K-1}\}$ (in $\mathrm{J\,m^{-3}}$) of K components. It is expressed as:

$$\Omega(\boldsymbol{\phi}, \nabla\boldsymbol{\phi}, \boldsymbol{\mu}) = \Omega_{\text{int}} + \Omega_{\text{bulk}} = \int_V \left[\underbrace{\frac{1}{\epsilon}\omega(\boldsymbol{\phi}) + \epsilon a(\boldsymbol{\phi}, \nabla\boldsymbol{\phi})}_{\text{int}} + \underbrace{\psi(\boldsymbol{\phi}, \boldsymbol{\mu})}_{\text{bulk}} \right] \mathrm{d}V. \quad (1)$$

Here, $\omega(\boldsymbol{\phi})$ is the multi-obstacle potential (in $\mathrm{J\,m^{-2}}$) and $a(\boldsymbol{\phi}, \nabla\boldsymbol{\phi})$ is the gradient energy density (in $\mathrm{J\,m^{-4}}$), both contributing to interfacial energy. The parameter ϵ (in meters) controls the interface thickness. In the present work, ϵ is treated as a diffuse-interface regularization parameter rather than as an independently calibrated physical interface thickness. Within the grand-potential formulation, it arises from the balance between the obstacle-potential and gradient-energy contributions in Eq. (1), and therefore sets the thickness of the diffuse metal-brine interface. Its value was chosen relative to the mesh so that the interface remains adequately resolved while keeping the computations tractable. For the corrosion validation cases, we retain $\epsilon = 5\,\mu\mathrm{m}$ from the benchmark configuration of Mai et al. [27] and Zhi et al. [35], while in the qualitative multiphase alloy simulations we use $\epsilon = 4\Delta x$. Keeping ϵ fixed within each simulation set ensures that differences in pit evolution arise primarily from microstructure and interfacial properties rather than from changes in interface regularization. The gradient term is defined as:

$$a(\boldsymbol{\phi}, \nabla\boldsymbol{\phi}) = \sum_{\alpha<\beta}^{N,N} \gamma_{\alpha\beta} |\boldsymbol{q}_{\alpha\beta}|^2, \tag{2}$$

where $\boldsymbol{q}_{\alpha\beta} = \phi_\alpha \nabla\phi_\beta - \phi_\beta \nabla\phi_\alpha$ is the generalized gradient vector orthogonal to the α-β interface. $\gamma_{\alpha\beta}$ represents the interfacial energy of the α-β interface. The potential $\omega(\boldsymbol{\phi})$ is:

$$\omega(\boldsymbol{\phi}) = \begin{cases} \left(\dfrac{16}{\pi^2} \displaystyle\sum_{\alpha\beta} \gamma_{\alpha\beta}\, \phi_\alpha \phi_\beta + \sum_{\alpha\beta\delta} \gamma_{\alpha\beta\delta}\, \phi_\alpha \phi_\beta \phi_\delta \right), & \text{if } \boldsymbol{\phi} \in \mathcal{G} \\ \infty, & \text{otherwise.} \end{cases} \tag{3}$$

Here, $\mathcal{G} = \{\sum_{\alpha=1}^{N} \phi_\alpha = 1, \phi_\alpha \geq 0 \forall \alpha \in \{1 \cdots N\}\}$ is the Gibbs simplex [36]. The ternary term ($\gamma_{\alpha\beta\delta}$) prevents third-phase formation at binary interfaces. The chemically interpolated grand potential density is given by:

$$\psi(\boldsymbol{\phi}, \boldsymbol{\mu}) = \sum_{\alpha=1}^{N} \psi_\alpha(\boldsymbol{\mu}) h_\alpha(\boldsymbol{\phi}), \tag{4}$$

with

$$\psi_\alpha(\boldsymbol{\mu}) = f^\alpha(\mathbf{c}^\alpha(\boldsymbol{\mu})) - \sum_{i=1}^{K-1} \mu_i c_i^\alpha(\boldsymbol{\mu}). \tag{5}$$

Here, f^α is the Helmholtz free energy of phase α, and $\mathbf{c}^\alpha = \{c_1^\alpha, c_2^\alpha, \dots, c_{K-1}^\alpha\}$ is the composition vector in that phase. From the phase-dependent $\mathbf{c}^\alpha$, an interpolated composition $\mathbf{c} \equiv \{c_1, \dots, c_{K-1}\}$ is written as:

$$c_i = \sum_{\alpha=1}^{N} c_i^\alpha h_\alpha(\boldsymbol{\phi}), \quad \forall 1 \leq i \leq K-1. \tag{6}$$

We use $h_\alpha(\boldsymbol{\phi}) = \phi_\alpha$ as the interpolation function, which satisfies the constraint $\sum_{\alpha=1}^{N} h_\alpha(\boldsymbol{\phi}) = 1$. Assuming local quasi-equilibrium, the chemical potential is equal across coexisting phases:

$$\mu_i = \frac{\partial f^\alpha(\boldsymbol{c}^\alpha)}{\partial c_i^\alpha} = \frac{\partial f^\beta(\boldsymbol{c}^\beta)}{\partial c_i^\beta} = \cdots = \frac{\partial f^N(\boldsymbol{c}^N)}{\partial c_i^N}. \tag{7}$$

The temporal evolution of the interpolated composition for the component i can be expressed as:

$$\dot{c}_i = -\nabla \cdot \boldsymbol{j}_i, \tag{8}$$

where $\boldsymbol{j}_i$ is the corresponding flux. Rewriting Eq. (8) with the help of Eq. (6) and using the product rule, we have,

$$\dot{c}_i = \sum_{\alpha=1}^{N} \dot{h}_\alpha(\boldsymbol{\phi})\, c_i^\alpha(\boldsymbol{\mu}) + \sum_{\alpha=1}^{N} h_\alpha(\boldsymbol{\phi})\, \dot{c}_i^\alpha(\boldsymbol{\mu}), \tag{9}$$

the evolution of chemical potential is obtained by inverting each $\dot{c}_i^\alpha(\boldsymbol{\mu})$, in favor of $\dot{\boldsymbol{\mu}}$ as,

$$\dot{\mu}_i = \left[\sum_{\alpha=1}^{N} h_\alpha(\boldsymbol{\phi}) \frac{\partial c_j^\alpha(\boldsymbol{\mu})}{\partial \mu_i} \right]^{-1} \left[\dot{c}_j - \sum_{\alpha=1}^{N} c_j^\alpha(\boldsymbol{\mu})\, \dot{h}_\alpha(\boldsymbol{\phi}) \right]. \tag{10}$$

The evolution of the order parameter is governed by

$$\frac{\partial \phi_\alpha}{\partial t} = -\frac{M_{\alpha\beta}}{2\epsilon} \left(\frac{\delta \Omega_{\mathrm{int}}}{\delta \phi_\alpha} - \frac{\delta \Omega_{\mathrm{int}}}{\delta \phi_\beta} + \frac{8\sqrt{\phi_\alpha(1-\phi_\alpha)}}{\pi} \Delta_{\mathrm{bulk}}^{\alpha\beta} \right), \tag{11}$$

where $M_{\alpha\beta}$ is the interface mobility coefficient of the $\alpha - \beta$ interface,

$$\Delta_{\mathrm{bulk}}^{\alpha\beta} = \frac{\delta \Omega_{\mathrm{bulk}}}{\delta \phi_\alpha} - \frac{\delta \Omega_{\mathrm{bulk}}}{\delta \phi_\beta}, \tag{12}$$

and

$$\frac{\delta(\cdot)}{\delta \phi_\alpha} := \frac{\partial(\cdot)}{\partial \phi_\alpha} - \nabla \cdot \frac{\partial(\cdot)}{\partial \nabla \phi_\alpha} \tag{13}$$

the variational derivative.

2.1.2. *Two-phase and two-component system*

To examine corrosion phenomena at a more computationally efficient and physically interpretable level, we now focus on a simplified binary system consisting of two phases and two components, representing the solid metal and the liquid electrolyte. The phase fields are collected in the vector $\boldsymbol{\phi} = \{\phi_s, \phi_\ell\}$, with the constraint $\phi_s + \phi_\ell = 1$. For the binary system, we denote the chemical potential vector as $\boldsymbol{\mu}$. Since only one component concentration is independent, this reduces to a single chemical potential, hereafter denoted simply as μ. While the previous section outlines the general grand-potential framework for multiphase and multicomponent systems, this reduced model isolates the essential mechanisms of corrosion at metal–electrolyte interfaces. It enables focused analysis of chemical potential gradients, interface motion, and mass transport, while also providing a computationally efficient platform for benchmarking and validation. Such simplification thus serves as a foundational basis for later multiphase extensions. In this binary solid–liquid case, the grand potential density can be expressed as,

$$\psi(\boldsymbol{\phi}, \boldsymbol{\mu}) = h(\phi)\psi_{\mathrm{s}}(\mu_{\mathrm{s}}) + (1 - h(\phi))\psi_{\mathrm{l}}(\mu_{\mathrm{l}}) = \phi_{\mathrm{s}}\psi_{\mathrm{s}}(\mu_{\mathrm{s}}) + (1 - \phi_{\mathrm{s}})\psi_{\mathrm{l}}(\mu_{\mathrm{l}}), \tag{14}$$

with

$$\psi_{\mathrm{s}}(\mu_{\mathrm{s}}) = f_{\mathrm{s}}(c'_{\mathrm{s}}(\mu_{\mathrm{s}})) - \mu_{\mathrm{s}} c'_{\mathrm{s}}(\mu_{\mathrm{s}}), \quad \psi_{\mathrm{l}}(\mu_{\mathrm{l}}) = f_{\mathrm{l}}(c'_{\mathrm{l}}(\mu_{\mathrm{l}})) - \mu_{\mathrm{l}} c'_{\mathrm{l}}(\mu_{\mathrm{l}}). \tag{15}$$

Here, the prime is indicating a normalization with the solid concentration, i.e., $c' := c/c_{\mathrm{solid}}$. Also this means, that c'_{s} and c'_{l} are the normalized concentrations of the co-existing solid and liquid phases, respectively. Assuming dilute solution thermodynamics, the free energy densities are,

$$f_{\mathrm{l}}(c'_{\mathrm{l}}) = A(c'_{\mathrm{l}} - c'_{\mathrm{le}})^2, \quad f_{\mathrm{s}}(c'_{\mathrm{s}}) = A(c'_{\mathrm{s}} - c'_{\mathrm{se}})^2. \tag{16}$$

Here, A is the free energy density curvature, which is assumed to be similar for both the solid and liquid phases. The value of A is computed such that the phase transformation driving force in the resulting approximate system is similar to that of the actual thermodynamic system. c'_{se} and c'_{le} are the normalized equilibrium concentrations for the solid and liquid phases respectively, and are given by,

$$c'_{\mathrm{se}} = \frac{c_{\mathrm{solid}}}{c_{\mathrm{solid}}} = 1, \quad c'_{\mathrm{le}} = \frac{c_{\mathrm{sat}}}{c_{\mathrm{solid}}} \tag{17}$$

with the saturation concentration c_{sat}. The chemical potential thus becomes,

$$\mu = \mu_{\mathrm{l}} = \mu_{\mathrm{s}} = \frac{\partial f_{\mathrm{l}}(c'_{\mathrm{l}})}{\partial c'_{\mathrm{l}}} = \frac{\partial f_{\mathrm{s}}(c'_{\mathrm{s}})}{\partial c'_{\mathrm{s}}}. \tag{18}$$

Hence,

$$c'_{\mathrm{l}}(\mu_{\mathrm{l}}) = \frac{\mu_{\mathrm{l}}}{2A} + c'_{le}, \quad c'_{\mathrm{s}}(\mu_{\mathrm{s}}) = \frac{\mu_{\mathrm{s}}}{2A} + c'_{se}. \tag{19}$$

Interpolated total concentration,

$$c'(\mu, \phi) = \phi_{\mathrm{s}} c'_{\mathrm{s}}(\mu) + (1 - \phi_{\mathrm{s}}) c'_{\mathrm{l}}(\mu). \tag{20}$$

The Cahn-Hilliard equation governs the conserved concentration field,

$$\frac{\partial c(\boldsymbol{x}, t)}{\partial t} = \nabla \cdot \left(\bar{M}(\phi) \nabla \mu \right). \tag{21}$$

Here $\bar{M}(\phi)$ is the mobility, which relates the flux density with the gradient of the chemical potential. This reads

$$\bar{M}(\phi) = h(\phi)\bar{M}_{\mathrm{s}} + (1 - h(\phi))\bar{M}_{\mathrm{l}}, \tag{22}$$

For all phase-specific mobilities $\bar{M}_\alpha$, the following applies,

$$\bar{M}_\alpha = D_\alpha \frac{\partial c_\alpha(\mu)}{\partial \mu}, \tag{23}$$

$$\bar{M}_\alpha \nabla \mu = D_\alpha \nabla c_\alpha. \tag{24}$$

The phase-dependent mobility therefore combines diffusional transport and the local thermodynamic response of concentration to chemical potential. In the present framework, it should be interpreted as an effective phase-field descriptor of dissolution kinetics rather than as a standalone directly measurable electrochemical constant. In practice, these effective mobility parameters may be calibrated against experimentally measured observables such as pit-depth evolution, preferential phase dissolution, phase-selective pit morphologies, or electrochemical response under controlled environmental conditions. Substituting into Eq. (21), we obtain,

$$\frac{\partial c(\boldsymbol{x}, t)}{\partial t} = \nabla \cdot \left(h(\phi) D_{\mathrm{s}} \nabla c_{\mathrm{s}} + (1 - h(\phi)) D_{\mathrm{l}} \nabla c_{\mathrm{l}} \right). \tag{25}$$

Assuming that the diffusion of metal ions in the solid phase is negligible, it can be considered, $D_{\mathrm{s}} = 0$ and $D_{\mathrm{l}} = D$ as suggested also in the work of Mai et al. [27]. By applying the chain rule to Eq. (20) follows for the evolution equation of the chemical potentials,

$$\frac{\partial c(\mu, \phi)}{\partial \mu} \frac{\partial \mu(\boldsymbol{x}, t)}{\partial t} = \frac{\partial c(\boldsymbol{x}, t)}{\partial t} - \left((c_{\mathrm{s}}(\mu) - c_{\mathrm{l}}(\mu)) \frac{\partial h(\boldsymbol{x}, t)}{\partial t} \right). \tag{26}$$

The evolution of the chemical potential field μ can then be isolated as,

$$\frac{\partial \mu(\boldsymbol{x}, t)}{\partial t} = \left[h(\phi) \frac{\partial c_{\mathrm{s}}(\mu)}{\partial \mu} + (1 - h(\phi)) \frac{\partial c_{\mathrm{l}}(\mu)}{\partial \mu} \right]^{-1} \times \left(\nabla \cdot \bar{M}(\phi) \nabla \mu - \left(c_{\mathrm{s}}(\mu) - c_{\mathrm{l}}(\mu) \right) \frac{\partial h(\boldsymbol{x}, t)}{\partial t} \right). \tag{27}$$

This formulation allows the chemical potential to be the only conserved variable that evolves in time, simplifying numerical implementation. From μ, the local concentrations of each phase are recovered through their constitutive relations. This avoids artificial oscillations that often arise in models where concentration is interpolated across interfaces. The model is robust and extensible to systems with multiple solid phases and grain boundaries, as elaborated by Hoffrogge et al. [37]. Thus, it serves as a solid foundation for simulating corrosion in metallic environments.

2.2. *Application of pressure on the diffuse liquid–solid interface*

To impose mechanical boundary conditions on an internal surface in a phase-field framework, we begin with the momentum balance formulated over the entire domain $V = V_{\mathrm{s}} \cup V_{\mathrm{v}}$ assuming quasi-static conditions (negligible inertia and body forces). This includes both the material (solid) region V_{s} and the void (non-material) region V_{v}. The formulation employs an indicator function I, which takes the value 1 in the solid domain and 0 in the void.

2.2.1. *Whole-domain momentum balance*

Following the procedure from [38], the strong form of the momentum balance can be expressed in a whole-domain formulation with stress boundary conditions. Starting from the weak form of the momentum balance and exploiting that the stress at the solid-void interface ∂V_{s} is the prescribed boundary traction tensor $\boldsymbol{\sigma}_{\mathrm{bc}}$, we obtain

$$\begin{aligned} 0 &= \int_{V_{\mathrm{s}}} -\boldsymbol{\sigma} : \nabla \boldsymbol{v} \, \mathrm{d}V + \int_{\partial V_{\mathrm{s}}} -\boldsymbol{\sigma}_{\mathrm{bc}} \boldsymbol{n} \cdot \boldsymbol{v} \, \mathrm{d}S \\ &= \int_V -I \boldsymbol{\sigma} : \nabla \boldsymbol{v} + \delta_S \boldsymbol{\sigma}_{\mathrm{bc}} \boldsymbol{n} \cdot \boldsymbol{v} \, \mathrm{d}V. \end{aligned} \tag{28}$$

Herein, $\boldsymbol{v}$ is a vector valued test function, I the indicator function, $\delta_S := \|\nabla I\|$ the surface Dirac distribution, $\boldsymbol{n}$ the outward pointing unit normal, $\boldsymbol{\sigma}$ the Cauchy stress tensor, and $:$ denotes the double contraction in the direct tensor notation. The usage of the indicator function allows the extension of the volume integral from V_{s} to V, while the surface Dirac allows transforming the surface integral to a volume integral due to its localization property. Integration by parts, exploiting that $I = 0$ on ∂V, and demanding Eq. (28) to hold for arbitrary test functions $\boldsymbol{v}$, yields the strong form of the local momentum balance in a whole-domain formulation

$$\nabla \cdot (I \boldsymbol{\sigma}) - \boldsymbol{\sigma}_{\mathrm{bc}} \cdot \nabla I = \boldsymbol{0}, \tag{29}$$

$$\nabla \cdot (I \boldsymbol{\sigma}) + \boldsymbol{t}_{\mathrm{bc}} \, \delta_S \quad = \boldsymbol{0}, \tag{30}$$

The two forms are equivalent which can be shown using that ∇I points in interface normal direction and thus, can be written as

$$\nabla I = -\|\nabla I\| \, \boldsymbol{n} = -\delta_S \, \boldsymbol{n}. \tag{31}$$

Furthermore, the boundary traction vector $\boldsymbol{t}_{\mathrm{bc}} = \boldsymbol{\sigma}_{\mathrm{bc}} \boldsymbol{n}$ is determined using the lemma of Cauchy. When the applied boundary condition is purely hydrostatic (pressure loading), the boundary traction vector reduces to,

$$\boldsymbol{t}_{\mathrm{bc}} = -p \, \boldsymbol{n},$$

where p is the prescribed external pressure acting normally on the interface.

2.2.2. *Diffuse interface approximation*

In the phase-field framework, the sharp indicator function I is replaced by a continuous phase-field variable ϕ_{s}, which smoothly transitions between 1 (solid) and 0 (void) over a diffuse interface. The momentum balance then becomes,

$$\nabla \cdot (\phi_{\mathrm{s}} \boldsymbol{\sigma}) + \boldsymbol{t}_{\mathrm{bc}} \, \tilde{\delta}_S = \boldsymbol{0}, \tag{32}$$

where $\tilde{\delta}_S$ is a smooth approximation of the surface Dirac delta distribution δ_S. Several choices are commonly used for $\tilde{\delta}_S$, including $\tilde{\delta}_S = \|\nabla \phi_{\mathrm{s}}\|$, $\tilde{\delta}_S = 2\epsilon \, \|\nabla \phi_{\mathrm{s}}\|^2$, and $\tilde{\delta}_S = 6\phi_{\mathrm{s}}(1 - \phi_{\mathrm{s}}) \, \|\nabla \phi_{\mathrm{s}}\|$. Here, ϵ is the interfacial width parameter controlling the thickness of the diffuse interface. In this work, the last approximation is employed leading to $\boldsymbol{t}_{\mathrm{bc}} \tilde{\delta}_S = 6\phi_{\mathrm{s}}(1 - \phi_{\mathrm{s}}) p \, \nabla \phi_{\mathrm{s}}$. This diffuse formulation allows the application of stress boundary conditions without explicitly tracking the interface geometry, making it well-suited for complex evolving interfaces in solid-mechanics phase-field models. The Cauchy stress tensor can be determined by means of Hooke's law as $\boldsymbol{\sigma} = \mathbb{C}_{\mathrm{s}} : \boldsymbol{\varepsilon}$ if a single solid phase is considered, where $\boldsymbol{\varepsilon} = \frac{1}{2} \left(\nabla \boldsymbol{u} + \nabla^T \boldsymbol{u} \right)$ is the strain, $\boldsymbol{u}$ the displacement field, and $\mathbb{C}_{\mathrm{s}}$ the stiffness of the solid. In this case, $\nabla \cdot (\phi_{\mathrm{s}} \mathbb{C}_{\mathrm{s}} : \boldsymbol{\varepsilon})$ arises in Eq. (32), which is similar to a linearly interpolated mixture stiffness between two phases, where the void phase exhibits a zero phase-specific stiffness. Therefore, without a boundary pressure, this results in a similar equation like the commonly used approach for porous media employing interpolation with a zero stiffness phase cf. [39]. If multiple solid phases are considered, the interpolated Cauchy stress needs to be used yielding

$$\phi_{\mathrm{s}} \boldsymbol{\sigma} = \sum_{\alpha=1}^{N_{\mathrm{s}}} \phi^\alpha \, \boldsymbol{\sigma}^\alpha, \quad \phi_{\mathrm{s}} = \sum_{\alpha=1}^{N_{\mathrm{s}}} \phi^\alpha \tag{33}$$

with N_{s} being the number of solid phases and $\boldsymbol{\sigma}^\alpha$ the corresponding phase-specific stress.

2.3. *Phase-field based crack modeling*

To model crack growth in the solid phases, we introduce a scalar crack phase-field ϕ_c, ranging from 0 in intact material to 1 in fully broken regions and the displacement vector $\mathbf{u}$ describing the mechanical deformation field. Under small strain assumption, the strain tensor is given by $\boldsymbol{\varepsilon} = \frac{1}{2} \left(\nabla \boldsymbol{u} + \nabla^T \boldsymbol{u} \right)$. The total free energy of a multiphase heterogeneous material with N_s solid phases and a crack phase is formulated as a volume integral of the free energy density f over the domain V,

$$\mathcal{F}[\boldsymbol{\varepsilon}, \phi_c, \nabla\phi_c] = \int_V f \, \mathrm{d}V$$
$$= \int_V \Bigg[\underbrace{\sum_{\alpha=1}^{N_\mathrm{s}} \phi^\alpha \, f^\alpha_\mathrm{el}(\boldsymbol{\varepsilon}, \phi_c)}_{\text{Elastic strain energy density}} + \underbrace{\frac{1}{2} \sum_{\alpha=1}^{N_\mathrm{s}} \phi^\alpha \, G^\alpha_c \left(\epsilon_c \, |\nabla\phi_c|^2 + \frac{1}{\epsilon_c} \, w(\phi_c) \right)}_{\text{Crack surface energy density}} \Bigg] \, \mathrm{d}V \, . \tag{34}$$

The first term in the integral represents the elastic strain energy density of the multiphase solid obtained by interpolating the phase-specific elastic energy densities f^α_el using the solid phase-field ϕ_α corresponding to phase α. In order to prevent non-physical crack growth under compressive states, f^α_el is split into a positive (tensile) and a negative (compressive) part,

$$f^\alpha_\mathrm{el}(\phi_c, \boldsymbol{\varepsilon}^\alpha) = (1-\phi_c)^2 \left[f^\alpha_\mathrm{el}(\boldsymbol{\varepsilon}^\alpha) \right]^+ + \left[f^\alpha_\mathrm{el}(\boldsymbol{\varepsilon}^\alpha) \right]^- , \tag{35}$$

representing the tension-compression split for isotropic elastic stiffness, according to Miehe et al. [40]. The positive and negative parts are given by

$$\left[f^\alpha_\mathrm{el}(\boldsymbol{\varepsilon}^\alpha) \right]^\pm = \frac{1}{2} \lambda^\alpha \langle \varepsilon^\alpha_1 + \varepsilon^\alpha_2 + \varepsilon^\alpha_3 \rangle^2_\pm + \mu^\alpha \sum_{i=1}^{3} \langle \varepsilon^\alpha_i \rangle^2_\pm \, , \tag{36}$$

in terms of the phase-specific Lame' parameters λ^α and μ^α, and the phase-specific principal strains $\varepsilon^\alpha_i \; \forall \, i \in \{1, 2, 3\}$. The scalar operator $\langle\rangle_\pm$ represents the Macaulay brackets defined as $\langle q \rangle_\pm = \frac{q \pm |q|}{2}$, q being any arbitrary scalar. The second term in the integral (Eq. (34)) represents the regularized crack surface energy density. Here G^α_c is the critical energy release rate of phase α, interpolated across all solid phases using summation. The regularization is achieved using the gradient term $\epsilon_c |\boldsymbol{\nabla}\phi_c|^2$ and the potential term $w(\phi_c)/\epsilon_c$, where $w(\phi_c) = \frac{9}{16}\phi_c$ is the obstacle type potential, and ϵ_c is a length-scale parameter that controls the width of the diffuse crack interface. Here, ϵ_c is the crack regularization length and therefore controls the intrinsic width of the diffuse crack zone. In all fracture simulations, we set $\epsilon_c = 3\Delta x$ with $\Delta x = 1\,\mu\mathrm{m}$, so that the ratio $\epsilon_c/\Delta x$ remains fixed across all cases. This choice allows a consistent comparison of the effect of pit morphology on crack initiation under the same numerical regularization. Accordingly, the fracture results are interpreted as comparative trends at fixed $\epsilon_c/\Delta x$, rather than as mesh-converged, material-specific crack-initiation thresholds. It should be noted that ϵ_c denotes the model regularization length, not the apparent width of the damaged band in post-processed fields, which may extend over more grid cells depending on the threshold used to define the crack region and the direction along which the width is measured. A dedicated sensitivity and convergence study with systematic variation of Δx and ϵ_c would be required to establish mesh-converged quantitative crack-initiation thresholds, such an analysis is beyond the scope of the present work. The effective stress is formulated as a linear interpolation according to Eq. (33) using the phase-specific stresses $\boldsymbol{\sigma}^\alpha = \mathbb{C}^\alpha : \boldsymbol{\varepsilon}$, using the Voigt/Taylor homogenization scheme [41].

Crack phase-field evolution. The crack order parameter ϕ_c evolves according to an Allen–Cahn type equation that drives the system towards minimal energy. The evolution equation is given by,

$$\begin{aligned}
\epsilon_c \frac{\partial\phi_c}{\partial t} &= - M_c \frac{\delta\mathcal{F}}{\delta\phi_c} \\
&= - M_c \left(\frac{\partial f}{\partial\phi_c} - \nabla \cdot \frac{\partial f}{\partial(\nabla\phi_c)} \right) \\
&= M_c \Bigg[\underbrace{- \sum_{\alpha=1}^{N_\mathrm{s}} \phi^\alpha \frac{\partial f^\alpha_\mathrm{el}(\boldsymbol{\varepsilon}, \phi_c)}{\partial\phi_c}}_{\text{Crack driving force } \mathcal{H}} - \frac{1}{\epsilon_c} \frac{\partial\omega(\phi_c)}{\partial\phi_c} \\
&\quad + \nabla \cdot \left(\sum_{\alpha=1}^{N_\mathrm{s}} \phi^\alpha \, G^\alpha_c \, \epsilon_c \, \nabla\phi_c \right) \Bigg] \, .
\end{aligned} \tag{37}$$

where M_c is a kinetic mobility parameter ($M_c \geq 0$) and $\delta\mathcal{F}/\delta\phi_c$ is the variational derivative of the free energy functional with respect to ϕ_c. The crack driving force $\mathcal{H}$, corresponding to the first term in Eq. (37), is defined as

$$\mathcal{H} = 2(1-\phi_c) \sum_{\alpha=1}^{N_\mathrm{s}} \left[f^\alpha_\mathrm{el}(\boldsymbol{\varepsilon}^\alpha) \right]^+ \phi_\alpha , \tag{38}$$

while the effective compressive energy density, obtained from the negative part in Eq. (35), is

$$f^-_\mathrm{el} = \sum_{\alpha=1}^{N_\mathrm{s}} \phi_\alpha \left[f^\alpha_\mathrm{el}(\boldsymbol{\varepsilon}^\alpha) \right]^- . \tag{39}$$

Momentum balance with applied pressure at the diffuse interface. Incorporating the degradation $h(\phi_c)$ due to the crack field and using linear interpolation of solid stresses (Eq. (33)), the momentum balance in the present phase-field framework becomes

$$\nabla \cdot \left(h(\phi_c) \sum_{\alpha=1}^{N_\mathrm{s}} \phi^\alpha \, \boldsymbol{\sigma}^\alpha \right) = -p \, \tilde{\delta}_S \, \boldsymbol{n} \, , \tag{40}$$

where the left-hand side represents the divergence of the effective stress in the solid and the right-hand side accounts for applied pressure at the diffuse interface. The phase-specific stress is determined by $\boldsymbol{\sigma}^\alpha = \mathbb{C}^\alpha : \boldsymbol{\varepsilon}$ using a Voigt–Taylor homogenization scheme which assumes all phase-specific strains to be identical. The crack degradation function reads,

$$h(\phi_c) = \begin{cases} (1-\phi_c)^2, & \text{if } 1-\phi_c > \phi_\mathrm{th} \\ \phi^2_\mathrm{th}, & \text{else.} \end{cases} \tag{41}$$

that ensures a smooth degradation of stresses where the crack phase is present, while maintaining a residual stiffness where the solid phase field is below a threshold ϕ_th. p is the applied fluid pressure (e.g. at the brine-solid surface) treated here as a distributed volumetric source term, $\boldsymbol{n}$ is the local unit normal vector pointing outward from the solid into the fluid (i.e. along the direction of pressure action), and $\tilde{\delta}_S$ is a smoothly localized approximation of the Dirac delta distribution that serves to confine the pressure loading to the diffuse solid–fluid interface. Detailed derivation of the formulation application of pressure at the diffuse interface is provided in Section 2.2. The crack evolution Eq. (37) and the linear momentum balance Eq. (40) are solved in a staggered manner. The mechanical equilibrium is solved implicitly, while the phase-field evolution for the crack is discretized using an explicit Euler scheme in time and central differences for spatial derivatives. A rotated staggered grid is used for discretization, with displacements stored at cell corners and phase fields and stresses evaluated at cell centers. These equations are solved iteratively at each (boundary or interface pressure) load increment until the crack phase-field reaches steady state.

The steady state is defined when the domain-averaged L_2-norm of the crack phase-field change falls below a tolerance ϵ_ss. As crack evolution is treated as a quasi-static process in the present staggered framework, the time steps associated with Eq. (37) represent numerical relaxation steps used to reach equilibrium under a given pressure increment, rather than physical propagation-time increments. At each relaxation step, the mechanical and phase fields are iteratively updated, and the irreversibility condition $\dot{\phi}_c \geq 0$ is enforced to prevent crack healing. For reducing computational costs, the material points exceeding a critical damage threshold $\phi^\mathrm{crit}_c = 1 - \epsilon_\mathrm{d}$ are assumed to be fully cracked and assigned $\phi_c = 1.0$, ϵ_d denoting the damage tolerance.

The presented phase-field crack model is an extension of the single crack order parameter (SCOP) model described in Schöller et al. [42] by incorporating the isotropic tension compression split [40] and accounting for the applied pressure at the diffuse interface within the linear momentum balance equation.

Importantly, the incorporation of a pressure boundary condition within the diffuse-interface mechanical framework is a novel aspect of this study (as discussed in detail in previous Section 2.2). To our knowledge, this approach has not previously been applied in phase-field corrosion–fracture models. It enables the simulation of fluid-induced stresses acting on corroding surfaces, providing a robust means to capture pressure-induced cracking in evolving geometries.

2.4. Modeling aspects

The present framework is subject to several modeling aspects and assumptions that define the scope of the results.

- Artificially increased diffusion coefficients are employed to reduce computational cost during pit evolution, while this approach preserves morphological trends, it alters absolute timescales. Consequently, the model is not intended to predict quantitative corrosion rates without calibration against experimental data.
- All simulations are performed in two dimensions, which restricts the representation of pit morphology, curvature evolution, and crack-tip/crack-front stress fields. Accordingly, the present work is intended as a mechanistic mesoscale study rather than as a direct quantitative prediction for three-dimensional engineering geometries. Extension to fully three-dimensional, experimentally informed microstructures is expected to improve quantitative realism while preserving the qualitative mechanisms identified in this study.
- Corrosion and fracture are modeled sequentially rather than through a fully coupled chemo-mechanical formulation. This reflects the intended separation between the slower evolution of pit morphology and the quasi-static equilibration of pressure-induced crack formation, but neglects feedback from local stress states to dissolution kinetics. Such feedback may become important in regimes involving stress-assisted dissolution, passive-film rupture/re-passivation, or stress-corrosion-sensitive chemistry at highly curved pit bases. The omission of this coupling is therefore non-conservative, for example, in cases where tensile stress accelerates localized dissolution, the present framework may overestimate the resistance to failure. The present formulation is thus intended for mechanistic mesoscale analysis of morphology-to-failure transitions rather than for fully coupled quantitative prediction in strongly chemo-mechanically interactive environments.
- Electrochemical processes are treated in a simplified manner, without explicit resolution of electric potential fields, charge transport, or re-passivation phenomena. Local chemistry effects beyond saturation-controlled dissolution are therefore not captured.
- The mechanical response is described using small-strain linear elasticity, with identical elastic properties assumed for all metallic phases. Plastic deformation, creep, hydrogen-assisted damage, and other inelastic mechanisms are not considered.
- Crack resistance is assumed to be homogeneous and phase-independent. Variations in fracture toughness between phases and environmentally assisted cracking mechanisms are not explicitly modeled.
- Pressure loading is applied quasi-statically and uniformly at the fluid–metal interface using a diffuse-interface formulation. Dynamic fluid–structure interaction effects, pressure gradients, and flow-induced loading are not included.
- The representation of multiphase alloys is limited to idealized microstructures and simplified interfacial mobility contrasts. Incorporating experimentally informed phase distributions, elastic heterogeneities, and measured brine chemistries would further improve predictive capability.

Table 1
Simulation parameter set for corrosion (Mai et al. [27]).

Parameter	Symbol	Value	Nondim. value
Interfacial energy	γ	$10\,\mathrm{J\,m^{-2}}$	1
Diffusion coefficient	D	$8.5\times10^{-10}\,\mathrm{m^2\,s^{-1}}$	4.25×10^{-5}
Interface mobility coefficient	M	$2\,\mathrm{m^3\,J^{-1}\,s^{-1}}$	1
Curvature of free energy density	A	$5.35\times10^{7}\,\mathrm{J\,mol^{-1}}$	5.35
Metal concentration	c_{metal}	$143\,\mathrm{mol\,L^{-1}}$	143
Saturation concentration	c_{sat}	$5.1\,\mathrm{mol\,L^{-1}}$	5.1
Interface thickness parameter	ϵ	$5\,\mu\mathrm{m}$	5

These modeling aspects do not affect the mechanistic conclusions drawn in this work, but they define the intended mesoscale scope of the framework and outline clear directions for future model refinement.

2.5. Model implementation

All simulations in this work were carried out using the in-house solver PACE3D [34] tailored for the decoupled multiphysics phase-field models described above. The code base is implemented in the C programming language and designed for high-performance computing applications. It utilizes the Message Passing Interface (MPI) standard for parallelization, incorporating domain decomposition and dynamic workload redistribution. This allows for efficient simulation of large-scale domains, including microstructures containing numerous grains or intricate interface geometries.

For reproducibility, the present simulations employed the grid resolutions, pressure increments, and convergence tolerances specified in the corresponding parameter tables. The mechanical equilibrium problem was solved implicitly within the staggered scheme, while the crack phase field was advanced by explicit relaxation steps until the domain-averaged L_2-norm of the crack-field change fell below the prescribed tolerance. All simulations were executed on a Linux-based high-performance computing (HPC) cluster. As representative computational context, the pseudo-1D and 2D validation simulations were executed on 200 and 800 CPU cores, respectively, with approximate wall-clock times of 72 h and 70 h. The qualitative corrosion simulations for multiphase pit evolution were typically run on 256 CPU cores with approximate runtimes of 9 h, while the fracture simulations were typically run on 10 CPU cores with approximate runtimes of 1–2 h. These values are reported to provide practical context for the computational cost of the present framework rather than as a formal benchmark against a fully coupled implementation.

3. Results and discussion

This section first validates the corrosion and mechanical formulations, and then presents simulation results for pit evolution and pressure-induced cracking in multiphase alloys. Section 3.1 benchmarks the phase-field corrosion model in pseudo-one-dimensional (1D) and two-dimensional (2D) configurations and verifies the diffuse stress boundary condition against analytical solutions. Section 3.2 then analyzes pitting corrosion and pressure-induced cracking in single-phase, dual-phase, and polycrystalline alloy systems, with particular emphasis on the roles of microstructure, interfacial energetics, and interfacial mobility.

3.1. Model validation

3.1.1. Validation of corrosion model

The simulation results are validated in both pseudo-one-dimensional and two-dimensional configurations by comparison with the benchmark study of Mai et al. [27] & Zhi et al. [35]. This provides a basis for assessing the model's accuracy in reproducing key features of corrosion phenomena. The parameters governing corrosion behavior are summarized in Table 1. These values are adapted from Zhi et al. [35], which compiles relevant data from experimental literature and established materials databases. For simulations conducted using Pace3D, all parameters are represented in non-dimensional form. Unless otherwise specified in individual simulation cases, the values listed in Table 1 are used consistently throughout. In particular, the interface-thickness parameter was kept unchanged for the validation study; $\epsilon = 5\,\mu\text{m}$ was retained from the benchmark setup in order to preserve direct comparability with the reference results.

Pseudo 1D pitting corrosion

The pseudo-one-dimensional configuration used in this study mirrors the simulation setup of the pencil electrode test described by Mai et al. [27]. A schematic illustration along with the associated boundary conditions is presented in Fig. 1a. In this model, a metallic wire with a diameter of $\text{d} = 25\,\mu\text{m}$ is embedded in an epoxy matrix, leaving only one circular face exposed to the surrounding electrolyte. It is assumed that at the initial moment ($t = 0$), a saturated salt layer rapidly forms on the exposed metal surface. This assumption allows the corrosion process to be treated as diffusion-controlled. The formation of this salt film is attributed to the application of a sufficiently high anodic potential, which activates electrochemical reactions at the metal–electrolyte interface. In the phase-field framework, the evolution of the system is captured without the need to explicitly track or impose boundary conditions at the corrosion front. Instead, boundary conditions are prescribed on the outer edges of the computational domain. Specifically, the interface between the metal and electrolyte (i.e., the exposed face of the wire) is assigned Dirichlet boundary conditions, where the normalized concentration of metal is set to $c' = 0$ and the corresponding phase field order parameter is initialized as $\phi = 0$ in the liquid phase. On the opposite end of the domain, representing the bulk region of the metal phase, fixed values of $c' = 1$ and $\phi = 1$ are applied. The lateral surfaces of the wire, encapsulated by the insulating epoxy, are modeled using Neumann boundary conditions (zero-flux) to ensure no mass or phase-field flux across these boundaries.

The pseudo-one-dimensional setup used in this study can effectively be approximated as a one-dimensional problem, since the dominant corrosion-driven metal dissolution occurs along the longitudinal axis of the wire. This simplification is consistent with analytical models [43] and previous numerical work, such as that by Mai et al. [27], who investigated similar configurations. To further evaluate the performance of our model, we compare our results with experimental data from Ernst et al. [44,45], as presented in the recent study by Zhi et al. [35]. These experimental results are not generated in the present work, but are used here as a reference dataset for validation of the corrosion model.

Although their simulations capture the general diffusion-controlled behavior, a noticeable deviation from the experimental trend is observed. This discrepancy, as discussed in [35], is primarily due to the limited thickness of the electrolyte domain used in their numerical setup. The reduced diffusion space constrains ion transport, resulting in an underestimation of the metal dissolution rate and consequently slower pit growth compared to experimental observations. Fig. 1b illustrates the ion concentration profiles in the electrolyte at various time steps from our simulation. These results confirm that the saturation condition at the metal-electrolyte interface ($c = c_{\text{sat}}$) is naturally fulfilled within the phase-field framework. Fig. 1c shows the evolution of pit depth (here, pit depth is defined as the maximum vertical distance between the initial metal surface and the deepest point of the corrosion pit at a given simulation stage) as a function of $\sqrt{t}$, comparing our results with (a) the analytical benchmark from [43], (b) numerical results from Mai et al. [27], and (c) experimental data from Ernst et al. and Zhi et al. [35,44,45]. Overall, the present simulation results show quantitative agreement with the analytical and numerical benchmarks, and captures the expected trend typical of diffusion-controlled processes. Future validation against replicate experimental datasets with uncertainty quantification would further strengthen the quantitative assessment of the model. The model demonstrates high predictive capability and provides a robust basis for future extensions to 2D pitting corrosion analysis.

2D pitting corrosion

To assess the predictive accuracy of the implemented phase-field framework for two-dimensional (2D) corrosion processes, we extended our 1D validation to a 2D pitting corrosion scenario. The setup follows the same geometric and physical assumptions as outlined by Zhi et al. [35], enabling a direct comparison with their benchmark study. The simulation domain consists of a metallic region in contact with an electrolyte (a liquid phase), partially covered by a protective coating. A localized opening in the coating initiates pit formation under a constant overpotential [35]. Dirichlet boundary conditions are applied along the exposed metal-electrolyte interface, with $c' = 0$ and $\phi = 0$ in the electrolyte region, while homogeneous Neumann boundary conditions are imposed at the lateral boundaries to reflect symmetry or insulation conditions (see Fig. 2a). The normalized concentration c' and electrochemical potential ϕ of the metal are initialized consistently with the configuration used by Zhi et al. [35]. All material properties and model parameters, including diffusivity, interface kinetics, and saturation concentration, are adopted directly from Zhi et al. [35] and Mai et al. [27] (Table 1) to maintain consistency and ensure a reliable basis for comparison. Unlike the full-domain approach employed in Zhi et al. [35] and other studies, our simulation restricts the electrolyte domain to the region within and immediately surrounding the pit, as shown in Fig. 2b. This is because our numerical framework (Pace3D) requires boundary conditions to be defined on the outer edges of the simulation domain. To compensate for the absence of a larger surrounding electrolyte volume, we assume that the electrolyte above the pit is continuously replenished by fluid flow, as would occur in real systems such as pipes or open channels. Therefore, the ion concentration at the pit mouth is effectively maintained.

Fig. 2b shows the temporal evolution of pit morphology as predicted by our 2D phase-field simulation, plotted at selected time steps (20 s, 35 s, 50 s, and 90 s). The distribution of the metal ion concentration illustrates the progression of the dissolution front as the corrosion pit propagates into the metal substrate. To quantitatively evaluate the simulation outcome, Fig. 2c compares the pit depth versus time obtained from our model with the published 2D simulation results of Zhi et al. [35]. Both datasets show a near-parabolic trend, characteristic of diffusion-controlled pitting corrosion. The close match between the two results confirms that our model accurately reproduces the interface motion and concentration-driven kinetics. It is worth noting that no artificial scaling of the concentration gradient or additional fitting parameters were introduced in our simulation. The agreement achieved is solely based on the physical transport of ionic species through diffusion as reported in their study, thereby validating the robustness and consistency of our implementation. The strong quantitative agreement between our results and those reported by Zhi et al. [35] validates our phase-field corrosion model as well as the underlying assumptions regarding the numerical setup, indicating that it is sufficient to capture the key mechanisms driving pit propagation.

3.1.2. Validation of the diffuse application of stress boundary condition

The diffuse application of the pressure boundary condition is validated using two benchmark elasticity problems. The first is an Euler–Bernoulli bending beam subjected to a uniform pressure load on its upper surface. The beam of length L and height H is embedded in a larger computational domain, and the pressure is applied through the diffuse-interface formulation of the momentum balance, Eq. (32). The corresponding analytical solution for the displacement, bending moment, and normal stress follows from classical beam theory and is

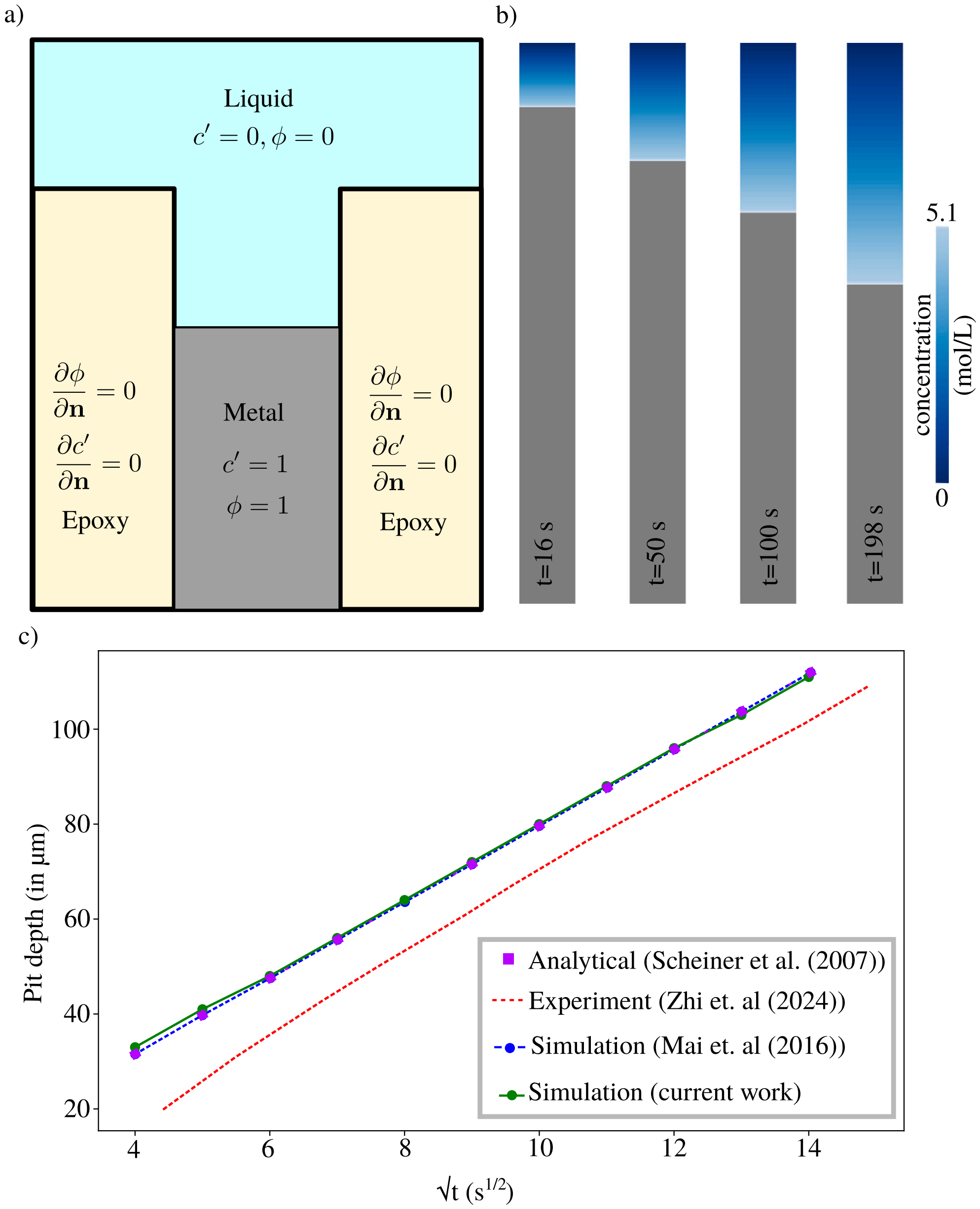

Fig. 1. Validation of the 1D phase-field corrosion model. (a) Schematic representation of the Pseudo-1D simulation setup. (b) Concentration profile at various time steps. (c) Comparison of pit depth versus $\sqrt{t}$ among different datasets: experimental measurements from Ernst et al. [44,45] as showcased in the work of Zhi et al. [35], analytical 1D solution provided by Scheiner et al. [46] and showcased in the work from Mai et al. [27] for numerical benchmarking, and the current study. Replicate-level uncertainty information was not available in the benchmark source used here.

summarized in Appendix A. The boundary conditions for the sharp- and diffuse-interface formulations are sketched in Fig. 3.

Numerical simulations are performed for a sequence of mesh refinements, with the beam discretized using $240\,r \times 20\,r$ cells in the x- and z-directions, where the refinement factor $r \in \{1, 2, 3, 4, 6\}$. The diffuse interface thickness δ is chosen as $\delta = 3.6\,\Delta z$, leading to $\delta/H = 0.18/r$. The extended domain above and below the beam is discretized accordingly. The normalized displacement $\tilde{w}$ and bending moment (torque) $\tilde{M}$ along the beam are used as benchmark quantities and are compared to the analytical solution (Fig. 4).

The convergence behavior is quantified using Richardson extrapolation [47,48], as outlined in Appendix B. Two extrapolated solutions are obtained: one using the three finest grids ($r = \{3, 4, 6\}$, denoted "ext, fine") and one using the intermediate set ($r = \{2, 3, 4\}$, denoted "ext, mid"). Fig. 4 shows the normalized displacement and torque for all refinements together with the extrapolated solutions and the analytical reference, while Table 2 reports the relative errors and estimated orders of accuracy. The numerical results exhibit monotonic convergence towards the analytical solution with an observed order of accuracy close to first order. The two extrapolated predictions differ by less than 1%, and both agree well with the analytical reference, indicating that the diffuse pressure boundary condition converges to the sharp-interface solution as the interface thickness decreases.

It is further observed that the torque exhibits smaller relative errors than the displacement, especially on coarser grids. This behavior is attributed to a slight overestimation of the geometrical moment of inertia in the diffuse-interface representation, which affects the displacement more strongly than the torque. A closed-form expression for the diffuse moment of inertia and its dependence on the interface thickness is derived in Appendix C and confirms that this error is intrinsic to diffuse-interface models and vanishes in the sharp-interface limit $\delta \to 0$.

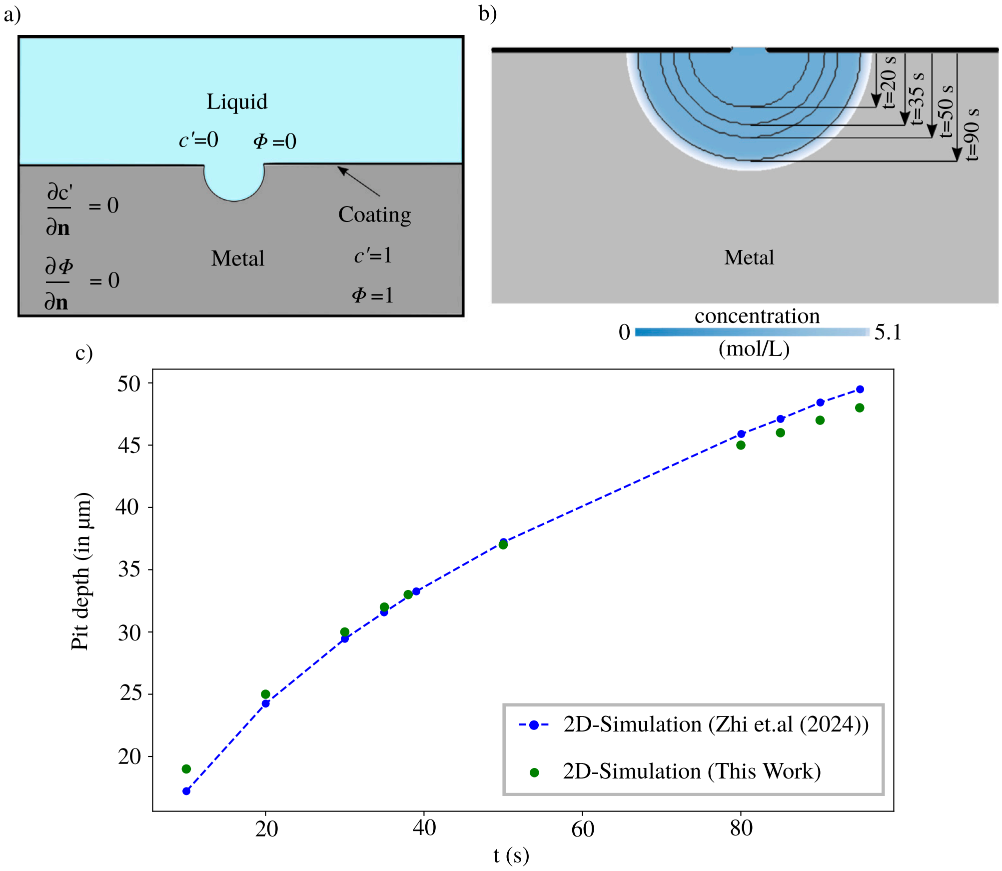

Fig. 2. Validation of the 2D phase-field corrosion model. (a) Schematic representation of the 2D simulation setup. (b) Concentration profile at various time steps. (c) Comparison of pit depth versus time (t) as showcased in the work of Zhi et al. [35] and the current study.

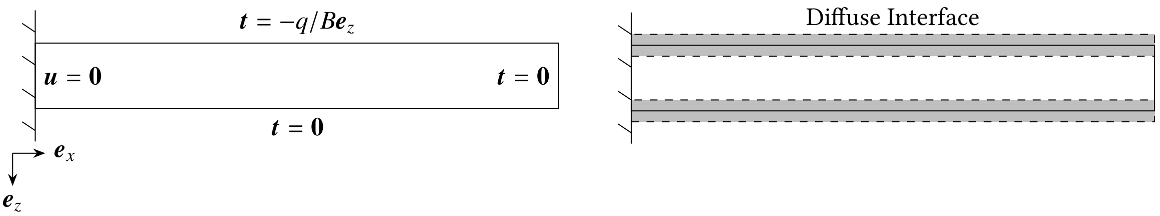

Fig. 3. Sketch of the Euler–Bernoulli bending beam used for validation. Left: Sharp interface with boundary conditions. Right: Diffuse interface at top and bottom where the stress boundary conditions are is diffusively applied.

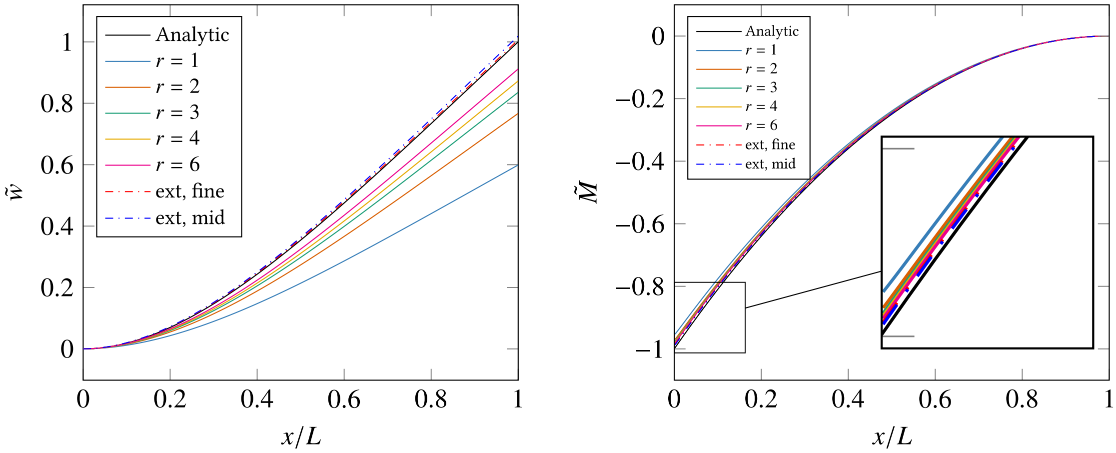

Fig. 4. Comparison of the analytical results for the normalized bending displacement $\tilde{w}$ and torque $\tilde{M}$ with the simulations and different refinements r. Additionally, the estimation using Richardson extrapolation is given by dash-dotted lines using the tuple $r = \{3,4,6\}$ (ext,fine) and $r = \{2,3,4\}$ (ext,mid), respectively.

Table 2
Comparison of the results for simulations and RE estimations compared to the analytical solution. Relative error e regarding the maximum bending $\tilde{w}(1)$ and torque $\tilde{M}(0)$ in % and estimated average order of accuracy $\hat{m}$ for the RE.

Displacement							
	$r = 1$	$r = 2$	$r = 3$	$r = 4$	$r = 6$	ext, mid	ext, fine
$\hat{m}(\tilde{w})$	–	–	–	–	–	0.7854	0.8521
$e(\tilde{w})$	40.1003	23.2980	16.4429	12.7341	8.8317	−1.8980	−0.6241
Torque							
	$r = 1$	$r = 2$	$r = 3$	$r = 4$	$r = 6$	ext, mid	ext, fine
$\hat{m}(\tilde{M})$	–	–	–	–	–	0.9614	1.2973
$e(\tilde{M})$	−4.7372	−3.0406	−2.4623	−2.1791	−1.9019	−1.2903	−1.5013

As a second benchmark, we consider a spherical stress state in which a solid ball of radius R is subjected to a uniform external pressure applied via the diffuse interface. The analytical solution corresponds to a homogeneous hydrostatic stress $\boldsymbol{\sigma} = p\mathbf{1}$ and strain $\boldsymbol{\varepsilon} = p/(3K)\mathbf{1}$, with K denoting the bulk modulus. Simulations are performed in a cubic domain of size $1.5R \times 1.5R \times 1.5R$, discretized with $100r$ cells per direction for $r \in \{1, 2, 4\}$, and an interface thickness $\delta = 4\,\Delta x$ (such that $\delta/R = 0.054/r$). The resulting spherical strains from the simulations are 0.9192%, 0.9532%, and 0.9710% from coarsest to finest grid, respectively, compared to the analytical value of 1%. Richardson extrapolation yields an extrapolated strain of 0.9906% with an estimated order of accuracy of 0.934. These results further confirm that the diffuse pressure boundary condition appropriately transfers fluid pressure onto the solid and reproduces the expected hydrostatic response with decreasing interface thickness.

Overall, the diffuse-interface formulation for applying a pressure boundary condition is shown to be accurate, first-order convergent, and stable across different mesh refinements. The close agreement with the analytical bending-beam reference and homogeneous spherical stress test confirms that the method reliably transmits fluid pressure to the solid domain. These results establish the mechanical robustness required for the subsequent corrosion–fracture simulations presented in Section 3.2.2.

3.2. Simulation-based results and analysis

Following the validation of the modeling framework, this section investigates pit evolution and failure in multiphase alloys under corrosive brine conditions. Section 3.2.1 explores pitting corrosion behavior in dual-phase and multiphase metallic systems using a qualitative modeling approach, with emphasis on the morphological evolution of pits across different alloy configurations. Section 3.2.2 examines pressure-induced crack growth at evolving corrosion pit surfaces in different microstructures, employing the pressure application method at the diffuse interface presented later in that section. Finally, we investigate the effect of differing corrosion kinetics, expressed as an interfacial mobility ratio, on failure behavior. The results show that variations in solid-phase reactivity with the electrolyte can intensify pit localization and lower the critical pressure for cracking in heterogeneous microstructures. These aspects are explored in the following subsections, providing a comprehensive view of pit evolution and structural degradation in complex alloy systems.

3.2.1. Pit morphology evolution in multiphase alloys: A qualitative analysis

In this analysis, the alloy components were selected based on the work of Zhi et al. [35]. The simulation domain spans $400\,\Delta x \times 160\,\Delta y$, where $\Delta x = \Delta y = 1\,\mu\mathrm{m}$ defines the uniform grid spacing. The simulations employed qualitatively selected parameters, with diffusion coefficients increased by six orders of magnitude (Table 3) to accelerate the pit growth process. For the qualitative multiphase corrosion simulations, ϵ was set to 4 in non-dimensional units, corresponding to $4\Delta x$, so that the diffuse corrosion front remained consistently resolved across all cases while allowing efficient long-time simulations. This scaling was necessary because fully quantitative modeling, even for single-phase systems, becomes computationally expensive within small simulation domains. Although the elevated diffusion coefficients do not reproduce the exact kinetics of material dissolution, they are expected to preserve the essential mechanisms of pit growth, yielding qualitatively similar morphologies. Simulations were conducted for two-phase alloy systems with varying phase configurations, horizontal, inclined, and vertical, as well as for a three-phase random polycrystalline alloy system (see Fig. 5). Furthermore, each binary interface, Fe–Brine, Fe–Al, Fe–Mn, Al–Brine, and Mn–Brine, was assigned a distinct interfacial energy parameter, scaled according to relative physical values. Table 3 summarizes all non-dimensional parameters used for the pitting corrosion simulations. In these simulations, the kinetic parameters were kept identical for all solid–liquid interfaces, while the interfacial energies varied, as listed in Table 3. Consequently, the evolution of corrosion pits is primarily governed by differences in interfacial energies. The microstructure further shapes pit morphology, as variations in interfacial energy influence phase-boundary angles and the kinetics at triple junctions, resulting in non-smooth pit morphologies at different stages for all configurations (see, Fig. 5). For the horizontal configuration, a symmetric pit morphology develops because the solid phases are arranged as horizontal layers perpendicular to the direction of pit growth. Since the Al–Brine interface has a lower interfacial energy than the Fe–Brine interface, pit growth is more pronounced in the Al phase, where dissolution is energetically favored. This trend is consistently observed across all two-phase configurations, indicating that differences in interfacial energy largely control the evolution of pit morphology. In these two-phase cases, the pit surface morphology varies with interfacial energy, whereas the pit depths remain comparable due to identical kinetics. In the three-phase random polycrystalline configuration, the Mn–Brine interface has the lowest interfacial energy among the three metal–brine interfaces. As a result, pitting is most pronounced in the Mn phase, as reflected in the simulated morphologies (last row in Fig. 5). In contrast to the two-phase systems, both pit morphology and depth are influenced in this case, reflecting the combined impact of randomly distributed solid phases and their differing interfacial energies. Overall, these findings highlight the dominant role of interfacial energy variations in controlling corrosion pitting, under identical solid–liquid kinetics, phases with the lowest metal–brine interfacial energy undergo preferential dissolution, ultimately dictating the morphology, depth, and localization of corrosion damage. In the later part of this discussion, we further analyze the influence of differing interfacial kinetics in these binary and polycrystalline alloy systems in addition to the differing interfacial energies (shown in Fig. 11), highlighting the role of kinetic variations on pit morphology evolution and subsequent crack formation.

3.2.2. Corrosion-driven failure via pressure-induced cracking in multiphase alloys

In this section, we investigate how corrosion pitting affects the mechanical integrity of various metallic microstructures under fluid

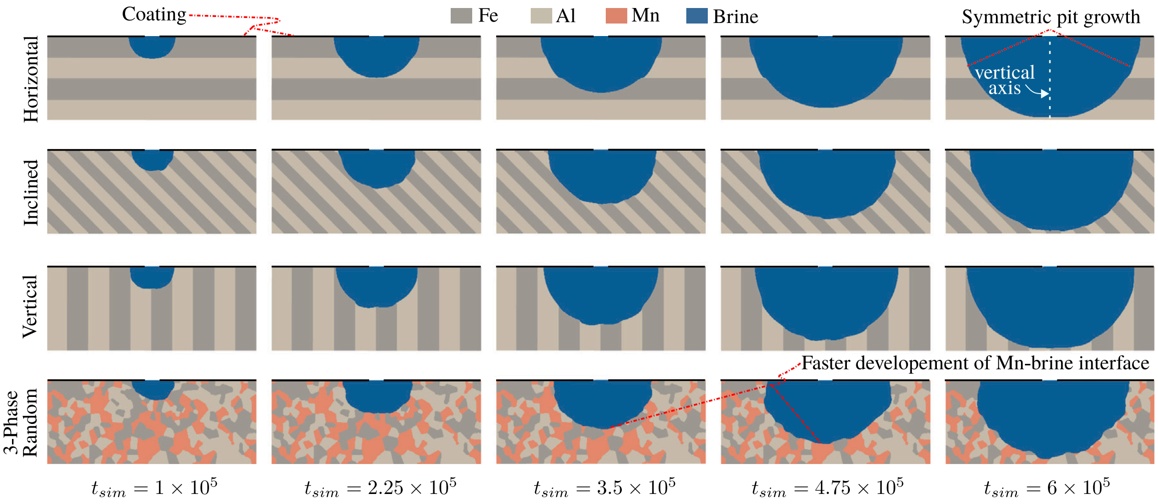

Fig. 5. Evolution of pit morphology in different alloy configurations for the 2-phase system and the 3-phase polycrystalline system. Inclined, vertical and polycrystalline system exhibit unsymmetric pit growth influenced by the phase-arrangement. [*On Top right*] Symmetric pit growth with respect to the vertical axis is observed in the horizontal configuration. [*In the bottom row*] The pronounced effect of surface energy is evident in the polycrystalline system for the Mn–Brine interface when compared to the Fe–Brine and Al–Brine interfaces.

Table 3
Non-dimensional (Non-dim.) parameter set for corrosion in multi-phase alloy system.

Parameter	Symbol	Non-dim. value
Interfacial energy (Fe-Brine)	$\gamma_{\text{Fe–Brine}}$	1
Interfacial energy (Al-Brine)	$\gamma_{\text{Al–Brine}}$	0.8
Interfacial energy (Mn-Brine)	$\gamma_{\text{Mn–Brine}}$	0.6
Interfacial energy (Fe-Al)	$\gamma_{\text{Fe–Al}}$	0.28
Interfacial Energy (Fe-Mn)	$\gamma_{\text{Fe–Mn}}$	0.32
Interfacial energy (Al-Mn)	$\gamma_{\text{Al–Mn}}$	0.32
Diffusion coefficient	D	10
Interface mobility coefficient	M	0.001
Curvature of free energy density	A	5.35
Metal concentration	c_{metal}	143
Saturation concentration	c_{sat}	5.1
Interface thickness parameter	ϵ	4

pressure. Building on the corrosion pitting simulations presented in the previous sections, we also perform additional corrosion pitting simulations in which the kinetic parameters differ for each metal–brine interface. Pit morphologies from all these simulations are extracted at representative stages and subjected to fluid pressure loading. This sequential treatment is intended to isolate the effect of pit morphology on crack-initiation susceptibility and therefore does not account for possible feedback of local stress states on the ongoing corrosion kinetics. Fracture mechanics simulations are then carried out using the mechanical phase-field fracture model described in Section 2.3 to assess the influence of pit depth and morphology on the critical fluid pressure required for crack initiation. Accordingly, the present analysis focuses on crack-initiation thresholds rather than on a full kinetic characterization of crack-growth evolution after initiation.

The numerical setup for the mechanical simulations applies the pressure at the diffuse solid–brine interface. All cases use the same domain geometry (400 μm × 180 μm) with uniform grid spacing ($\Delta x = \Delta y = 1\,\mu\text{m}$). In the simulated pit morphologies, we further add a thin brine layer above the metal phase, in order to enable uniform fluid pressure application along the solid-brine interface, illustrated in Fig. 6a. A smooth *diffuse-interface* pressure boundary condition is employed, as described in Section 3.1.2 and illustrated by the pressure field in the diffuse solid–liquid interface in Fig. 6b. The pressure is incrementally ramped up linearly (Fig. 6c) to determine the critical value for crack initiation. All material phases are assumed to have identical elastic stiffness in these simulations. While the model is capable of incorporating stiffness contrasts between phases via mechanical jump-conditions [49], this capability is not utilized in the present work for the sake of simplicity. Consequently, the scope of the present analysis is limited to investigating the influence of pit morphology on the critical pressure for crack initiation. Within this setting, the fracture response should therefore be interpreted in a brittle fracture framework, with emphasis on comparative morphology-to-failure trends rather than on alloy-specific ductile fracture prediction. Since, all solid phases are assigned identical elastic stiffness and homogeneous fracture resistance in the present implementation, effects such as crack deflection or crack arrest caused by phase-specific mechanical contrast are not captured here. Therefore, the predicted crack paths should be interpreted as pit-morphology-driven rather than phase-boundary-guided. Further, the thin coating layer present between the fluid and the metal is not considered due to its negligible thickness compared to the metal substrate and the complexity introduced by its distinct mechanical properties.

For all mechanical simulations, boundary conditions were chosen to prevent rigid-body motion and to identify the sites of stress localization, enabling analysis of the role of pit morphology in failure (Fig. 6a). Here, the right face of the domain has fixed x-displacement ($u_x = 0$), the top and bottom faces have fixed y-displacement ($u_y = 0$), and the left is traction-free ($\boldsymbol{\sigma} \cdot \mathbf{n} = 0$). The material properties and numerical parameters used for the mechanical simulations are summarized in Table 4. These parameters define the grid resolution, regularization length, pressure incrementation, and convergence settings used throughout the fracture calculations. The chosen values are representative and were selected to provide a stable and internally consistent brittle phase-field setting in which crack formation occurs within the small-strain regime assumed in the present model. Accordingly, the resulting absolute pressure values should be interpreted as simulation-based comparative quantities for analyzing morphology-to-failure trends, and not as direct quantitative failure predictions for a specific engineering alloy.

As corrosion pits deepen over time, stress concentrates at the sharp regions of the pit morphologies, reducing the material's resistance to cracking. In general, the critical pressure for crack initiation (p_{crit}) decreases as the pit grows larger (i.e., as the remaining ligament of sound material thins). This trend reflects progressive weakening of the structure. However, the relationship is not strictly monotonic, the pit shape plays a crucial role. Sharp pit features (e.g., corners or notches along the corrosion front) amplify local stress and can trigger cracking

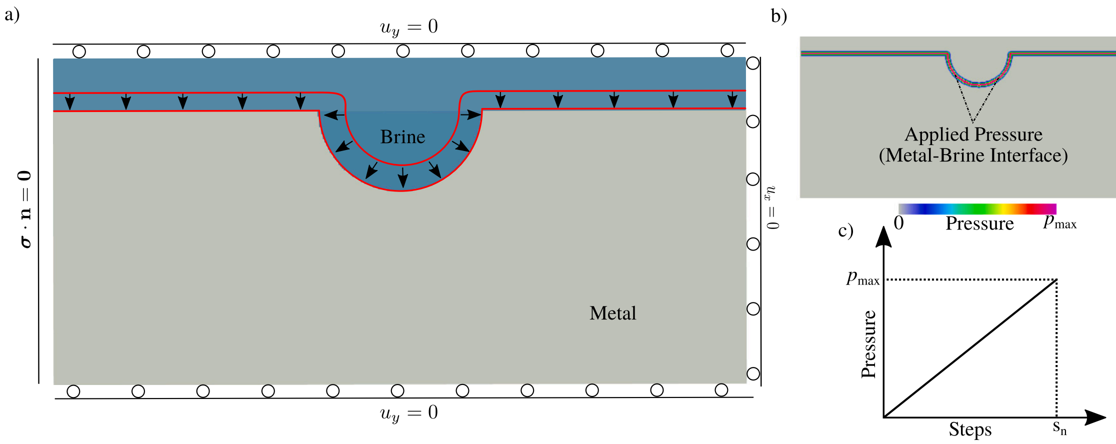

Fig. 6. Schematic representation of the boundary conditions used for modeling pressure-induced cracking during pit evolution. (a) Applied Neumann boundary condition on the left face and Dirichlet boundary conditions on the remaining faces of the domain, with pressure applied normal to the brine–metal interface. (b) Pressure distribution across the diffuse metal–brine interface. (c) Plot of applied pressure versus increment steps, showing linear ramping.

Table 4
Material and simulation parameters.

Parameter	Symbol	Value	Unit
Material parameters			
Young's modulus	E	210	GPa
Poisson's ratio	ν	0.3	–
Reference crack resistance	G_0	100	N/mm
Simulation parameters			
Mesh size	Δx	1	μm
Crack regularization length scale	ϵ_c	3	μm
Pressure incremental steps	Δp	1	MPa
Kinetic mobility parameter	M_c	10^{-3}	–
Residual stiffness factor	$\varphi_{\text{residual}}$	10^{-12}	–
Steady-state tolerance	ϵ_{φ_c}	5×10^{-5}	–
Damage tolerance	ϵ_{damage}	0.02	–

Note: The mechanical parameters are used here for comparative phase-field fracture analysis within a small-strain brittle fracture framework; absolute critical pressures should not be interpreted as direct engineering failure pressures.

at relatively lower pressures, whereas smoother, rounded pit profiles distribute stress more evenly and thus sustain higher pressures before failure. To enable a consistent comparison across time and different morphologies, we introduce the *normalized critical pressure* ($\hat{p}$):

$$\hat{p} = \frac{p_{\text{crit, current}}}{p_{\text{crit, max}}}$$

where $p_{\text{crit,current}}$ is the pressure at which crack initiation occurs at a given corrosion stage. The reference value $p_{\text{crit,max}}$ corresponds to the highest crack-initiation pressure observed in the earliest considered stage of corrosion for different cases, when pits were shallow and relatively smooth. The corresponding physical values of $p_{\text{crit,max}}$ used for normalization are reported in the relevant figure captions and vary depending on the comparison set considered in each case. This dimensionless metric indicates the relative loss of load-bearing capacity due to corrosion damage. In the present work, this quantity is used as the primary comparative metric because the main objective is to evaluate the onset of morphology-induced mechanical instability across different corrosion states and microstructures. Moreover, during the mechanical analysis, pit depth is used as the primary scalar descriptor because it provides a simple and physically interpretable measure of corrosion severity that is relevant to the assessment of crack initiation. A more detailed characterization of post-initiation crack evolution, such as crack length and propagation kinetics, is left for future work, since these quantities also depend on the pressure-incrementation strategy and phase-field relaxation procedure in the present quasi-static fracture model. The following sections present results for each case, highlighting the evolution of pit morphology, crack initiation, and mechanical response.

Metal–electrolyte system (Fe–Brine)

In this section, we analyze the simulated crack growth at different stages of corroded pit in a single-phase (iron) metal exposed to brine. Fig. 7 depicts crack initiation and propagation as the applied pressure is incrementally increased. The plot of normalized critical pressure versus pressure increment steps forms a straight line, reflecting the linear ramping of applied pressure, with the pressure increment size $\Delta p = 1$ MPa. The crack initiates at a critical pressure of 1499 MPa and continues to grow with subsequent pressure increments, as illustrated by a later stage at 2169 MPa. The inset in Fig. 7a shows contour plots of crack growth at the critical pressure 1499 MPa, the same pressure at which the crack first appeared, together with the effective compressive energy density showcasing the compressive component of the elastic strain energy density (see, Eq. (39)), which does not contribute to the crack driving force. Regions not dominated by compressive energy states act as potential crack nucleation sites. For this semi-circular pit, crack initiation occurs near the deepest part of the pit, where discrete steps (due to numerical discretization) create sharp notch-like features, and serve as potential crack nucleation sites. Initially, two potential nucleation sites form, but one becomes dominant, breaking the symmetry and driving further growth. This occurs because, although both sites experience elevated local stress concentration, their tensile crack-driving forces and surrounding ligament geometries are not identical. Crack propagation initiates at the site with the highest effective tensile driving force and the most severe local stress-concentrating geometry, after which the surrounding stress field is redistributed and suppresses competing propagation from neighboring sites. At a pressure of 2169 MPa, the inset plots in Fig. 7b show the crack driving force field, computed from the positive component of the elastic strain energy density (see, Eq. (38)), peaking at the crack tip and dictating the direction of crack propagation. Fig. 8(a–d) presents the simulated crack initiation and growth at representative stages of pit evolution. For these simulations, the normalized critical pressure ($\hat{p}$) is plotted as a function of pit depth. The results reveal a linear decrease in critical pressure with increasing pit depth, with a negative slope of $m_{\text{single}} = -0.005\,\mu\text{m}^{-1}$ obtained from linear regression. Despite the overall spherical pit morphology, cracks consistently initiate and propagate near the deepest part of the pit, where discrete steps, introduced by numerical discretization, introduce local geometric irregularities. These steps act as stress concentrators, providing preferential sites for crack nucleation at all stages of pit growth. Once initiated, cracks extend in directions dictated by the

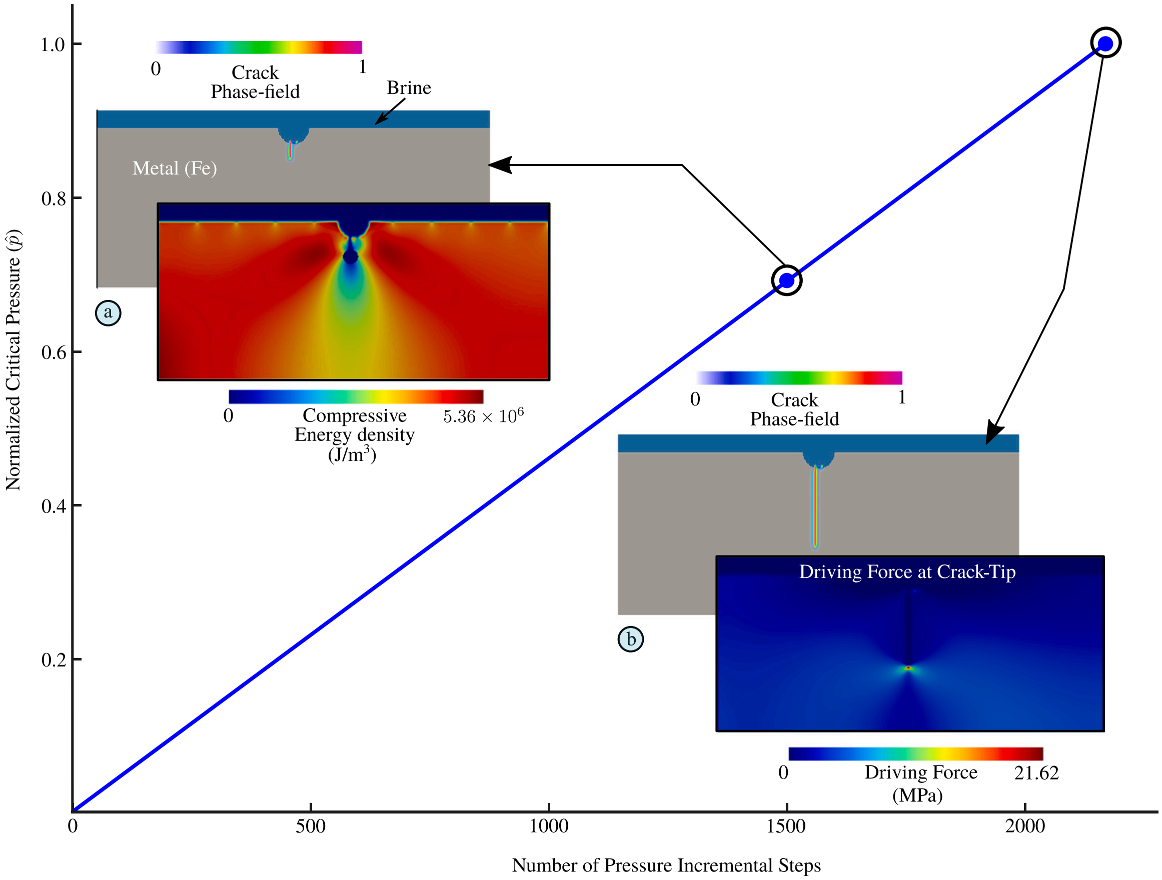

Fig. 7. Plot of the normalized critical pressure, $\hat{p} = p_{\text{crit,current}}/p_{\text{crit,max}}$, where $p_{\text{crit,max}} = 2169$ MPa for the Fe–Brine system, as a function of incremental pressure steps of step size $\Delta p = 1$ MPa. This absolute value serves as a simulation-based comparative reference pressure within the present brittle phase-field setting and should not be interpreted as a direct engineering failure pressure. (a) Contour plots of the crack phase-field and compressive energy density at $p = 1499$ MPa, illustrating crack growth during the early stage. (b) Contour plots of the crack phase-field and crack driving force at the later stage of $p = 2169$ MPa.

crack driving force, as shown in the inset of Fig. 7b. Since the pit maintains an almost spherical shape throughout the simulation, the reduction in critical pressure is predominantly governed by pit depth rather than shape evolution. This indicates that, for pits with minimal morphological change, depth alone can serve as a reliable predictor of the pressure required for crack initiation. In practical terms, even geometrically smooth corrosion pits can exhibit progressively lower resistance to pressure-induced fracture as they deepen, highlighting the need for early detection and mitigation before critical depths are reached.

Dual-phase alloy systems: Fe–Al in brine environment

Previous studies on dual-phase and layered metallic systems have demonstrated that the directionality and connectivity of microstructural features can strongly influence localized corrosion behavior and, consequently, crack sensitivity [14]. To examine how the simulated pit morphologies in the different dual-phase alloy systems described in Section 3.2.1 affect the critical pressure for crack initiation, additional simulations are conducted using the phase-field fracture model. The numerical setup is identical to that shown in Fig. 6, and the material and simulation parameters are as listed in Table 4. The alloy microstructures differ according to the considered configurations, Horizontal, Inclined, and Vertical layers, with pit growth evaluated at various stages. In each case, pressure is applied incrementally at the solid–liquid interface to determine the critical pressure at which crack initiation occurs.

Fig. 9(a–c) show the simulated crack initiation and subsequent propagation at different stages (simulation times t_{sim}) of pit growth for the horizontal, inclined, and vertical layer configurations. The corresponding plot of normalized critical pressure as a function of pit depth is presented in Fig. 9d.

Unlike the spherical pit morphologies observed in the single-phase cases, the pits in these dual-phase configurations exhibit irregular geometries with regions of high local curvature that act as stress concentration sites. Although several such locations may act as potential crack-initiation candidates, the dominant propagating crack emerges from the site with the highest local tensile driving force and most severe local stress-concentrating geometry. These irregularities arise from variations in metal–liquid interfacial energies between the constituent phases. However, their extent remains relatively consistent across all three configurations and throughout all stages of pit growth. As a result, the predicted critical pressures for the different configurations are similar at comparable stages.

At the initial stage ($t_{sim} = 1 \times 10^5$), the differences in critical pressure between the three cases are more pronounced. The horizontal configuration exhibits greater resistance to crack initiation, as its pit morphology remains nearly spherical and smooth due to pit growth occurring solely within the Fe phase. In contrast, the inclined and vertical configurations display local sharp features at the pit boundary, arising from simultaneous pit growth in both Fe and Al phases. As pit depth increases, the influence of local morphological differences diminishes, and the variation in critical pressure among the configurations decreases. This is because pit depth itself becomes the dominant factor governing the critical pressure for crack growth. Since pit depths are comparable across all configurations at later stages, the predicted critical pressures converge.

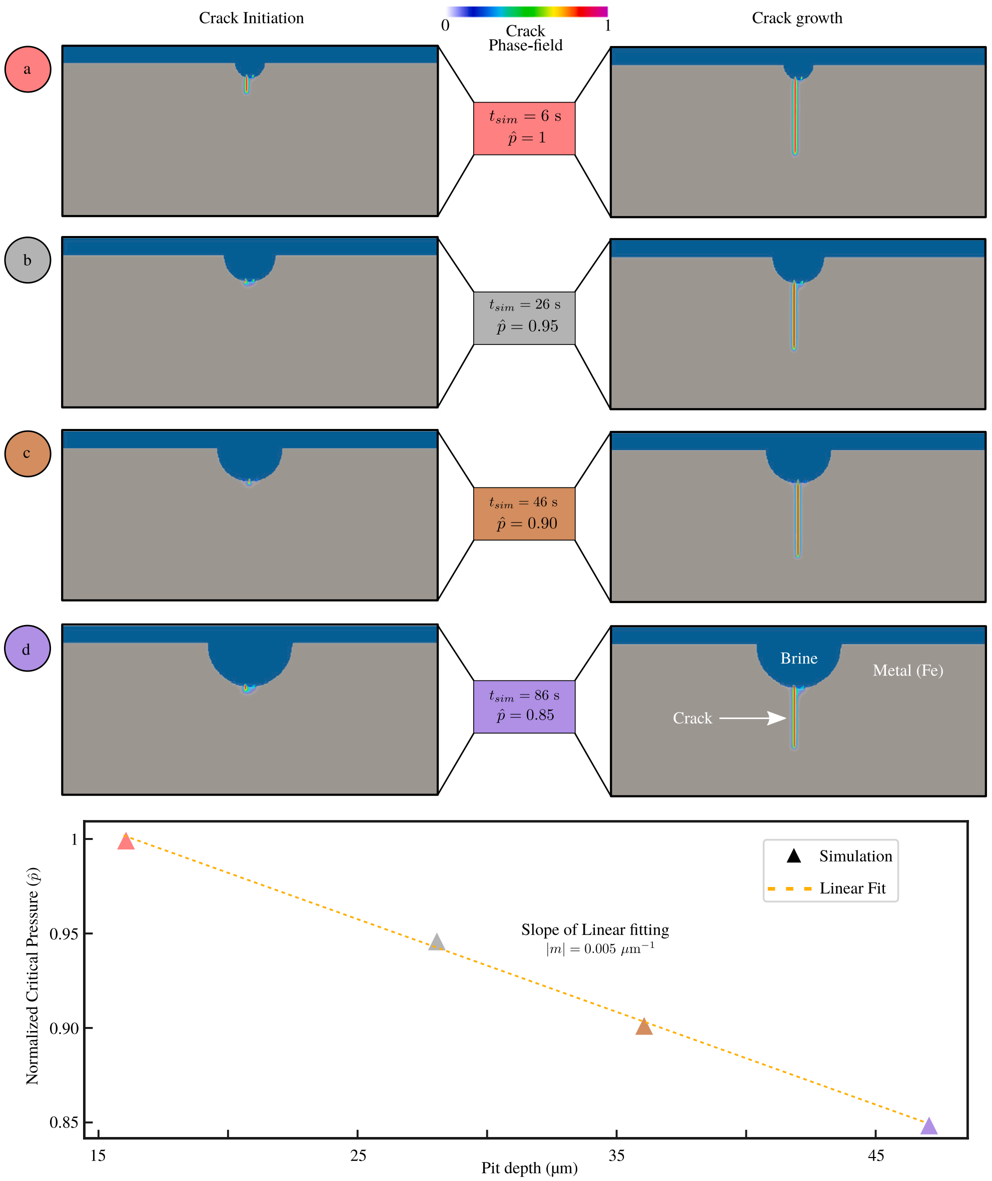

Fig. 8. (a–d) Simulated crack initiation (left column) and growth (right column) at representative stages of pit evolution in the Fe–Brine system. The below plot shows the normalized critical pressure as a function of pit depth (µm), where the normalization uses $p_{\mathrm{crit,max}}$ = 1499 MPa for the comparison set shown. The markers in the graph are color coded to represent different stages as shown in (a–d). The yellow dotted line indicates a linear fitting of the simulation datasets with a slope of $|m| = 0.005\ \mu\mathrm{m}^{-1}$.

At the final stage considered, the pit almost penetrates to the opposite side of the metallic layer (see Fig. 5 at $t_{sim} = 6 \times 10^5$), resulting in a negligible critical pressure for crack initiation in all configurations. Given that the physical wall thickness of an actual metal pipe system is much greater than the alloy thickness modeled here, these results should be interpreted as representing the qualitative trend of critical pressure variation with pit depth and morphologies, governed by the underlying dual phase structures, rather than as direct quantitative predictions. These results capture the qualitative patterns of critical pressure variation while isolating the influence of pit morphologies dictated by the underlying alloy microstructure.

Polycrystalline alloy system with multiple metal phases (Fe–Al–Mn + Brine)

Finally, we examine a three-phase alloy with a random polycrystalline microstructure composed of Fe, Al, and Mn phases in contact with brine. The domain and loading conditions are identical to those in the previous cases; however, the metal phases here are distributed irregularly, approximating a random grain structure rather than well-defined layers. No single phase forms a continuous path through the material, and phase boundaries intersect at various angles and locations. The presence of the additional Mn phase introduces new Mn–brine, Fe–Mn, Al–Mn interfaces, for which the interfacial energy is assigned as given in Table 3. All other simulation parameters are kept identical to those used in the preceding dual-phase alloy systems.

In this polycrystalline system, the pit evolves in a non-uniform manner due to the heterogeneous phase arrangement. Instead of maintaining a smooth spherical surface, the corrosion front develops an irregular morphology with regions of high curvature, as corrosion progresses more rapidly in certain phases compared to others (see, Section 3.2.1). Fig. 10(a–c) shows the simulated crack growth at representative stages of pitting. High-curvature regions of the pit act as

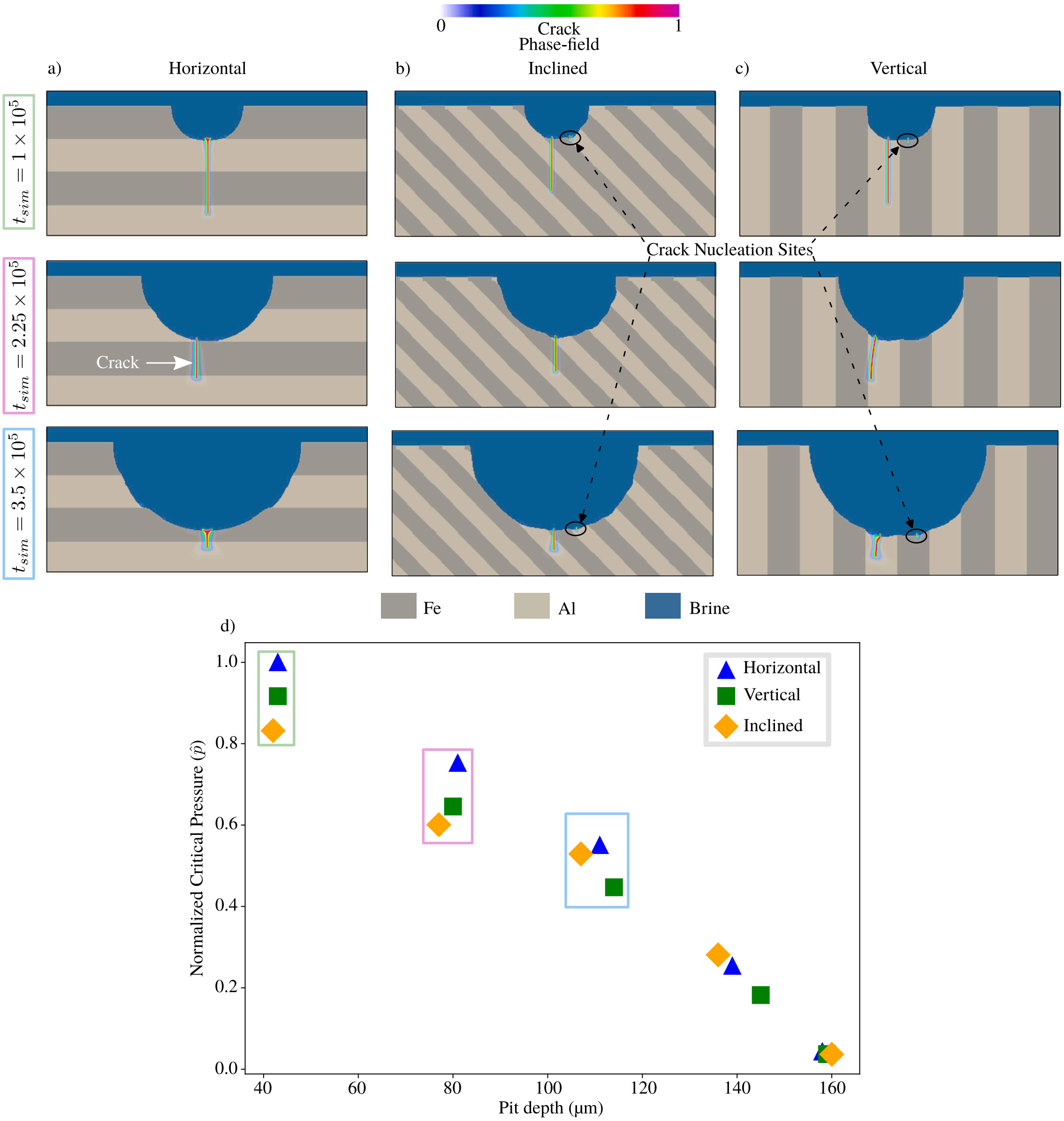

Fig. 9. Pressure-induced cracking in a two-phase Fe–Al alloy system with varying phase orientations: (a) horizontal, (b) inclined, and (c) vertical, at 3 different time steps, showcasing crack growth. (d) The graph illustrates the relationship between normalized critical pressure and pit depth, evolving over time, for each of the three orientation cases, where the normalization uses $p_{\text{crit,max}}$ = 1476 MPa for the comparison set shown.

stress concentration sites, making them preferred locations for crack nucleation and growth. Note that multiple nucleation sites can form, as observed in the figure. However, crack propagation predominantly occurs from the site with the most critical stress conditions, that is, the location where the combined effect of local pit-surface curvature, ligament geometry, and tensile crack-driving force is strongest. Once one crack begins to advance, stress redistribution reduces the likelihood of continued propagation from nearby competing nucleation sites.

We plot the normalized critical pressure $\hat{p}$ with the pit depth as shown in Fig. 10d. A near linear decline in $\hat{p}$ with the pit depth is observed with a fitted slope of $m_{\text{poly}} = -0.008\,\mu\text{m}^{-1}$. This trend arises because the irregularities in pit morphology, manifested as high-curvature regions, are consistently present throughout the simulation due to random polycrystalline grain structure. As a result, while the pit deepens over time, the degree of morphological irregularity remains largely the same, making pit depth the dominant factor governing the critical pressure for crack initiation. It is worth noting that if the initial stages of pitting had featured sharp notches, these could have acted as severe stress concentrators, triggering crack initiation and subsequent failure at lower critical pressures.

It is noteworthy that pitting in the single-phase Fe–Brine system (see,) and in the polycrystalline system considered here both exhibit a near-linear decline in critical pressure with increasing pit depth. However, the decline in the latter case is noticeably steeper ($|m_{\text{poly}}| > |m_{\text{single}}|$), indicating that the critical load decreases more rapidly with pitting in polycrystalline microstructures. This behavior is attributed to the persistent surface irregularities of the pit morphology at the same depth in the polycrystalline case, which act as additional stress concentrators and accelerate the loss of load-bearing capacity.

Effect of interfacial mobility ratio on failure response

Analysis overview. In the previous sections, all pit growth simulations were performed with identical interfacial kinetics for all metal–brine interfaces, focusing solely on the impact of differing interfacial energies on pit evolution. In this section, we systematically investigate the effect of differing corrosion kinetics between ferritic (Fe) and non-ferritic

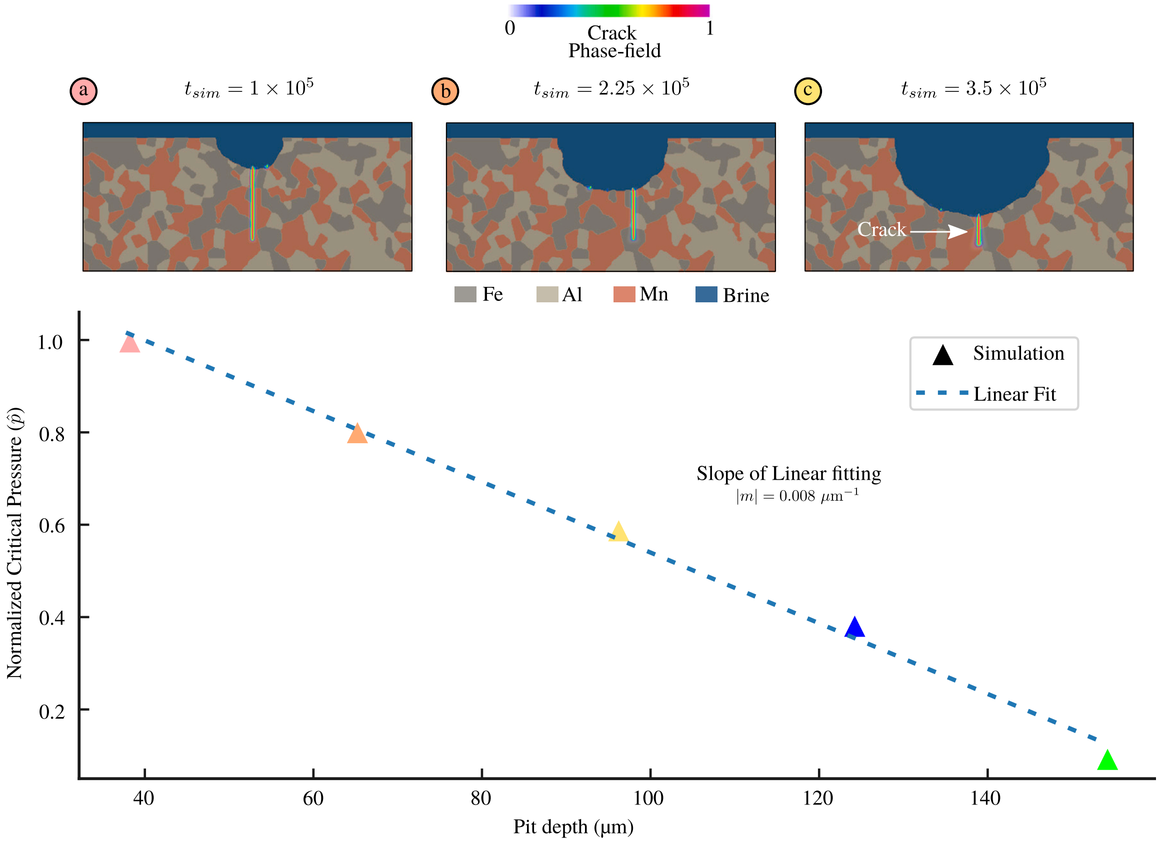

Fig. 10. (a–c) Simulated crack growth at representative stages of pit evolution in the polycrystalline system. (d) The below plot shows the normalized critical pressure as a function of pit depth (µm), where the normalization uses $p_{\text{crit,max}}$ = 1374 MPa for the comparison set shown. The markers in the graph are color coded to represent different stages as shown in (a–c). The blue dotted line indicates a linear fitting of the simulation datasets with a slope of $|m|$ = 0.008 µm^{-1}.

(Mn, Al) phases by introducing the interfacial mobility ratio parameter,

$$\bar{M}_\mathrm{R} = \frac{\bar{M}_\mathrm{ferrite}}{\bar{M}_\mathrm{non\text{-}ferrite}}. \tag{42}$$

The parameter is varied in the set $\bar{M}_\mathrm{R} \in \{1, 2, 4, 8\}$ by adjusting the mobility of the non-ferrite phase $\bar{M}_\mathrm{non\text{-}ferrite}$, while keeping the ferrite-phase mobility $\bar{M}_\mathrm{ferrite}$ constant. Increasing $\bar{M}_\mathrm{R}$ decreases the corrosion kinetics of the non-ferrite phase, consistent with experimental observations for Fe–Mn–Al alloys [50], where ferrite preferentially corrodes due to its lower passivation stability. The simulated pit growth and resulting crack growth due to the application of pressure on the metal-brine diffuse interface at an intermediate stage ($t_{sim} = 3.5 \times 10^5$) for different mobility ratios is presented in Fig. 11(a–d) for four distinct microstructural configurations: dual-phase arrangements with horizontal, vertical, and inclined interfaces, and a randomly distributed three-phase polycrystalline system. The influence of the mobility ratio on pit depth, normalized critical pressure ($\hat{p}$), and pit surface-to-volume ratio is further analyzed in Fig. 11(e–g). Although dissolved area is also a useful descriptor of corrosion extent, especially for irregular pit morphologies, it does not necessarily evolve proportionally with pit depth when pit growth involves strong lateral spreading, grooves, or lobe formation. Pit depth is used here as the primary scalar measure because it provides a simple and physically interpretable descriptor of corrosion severity that is relevant to the assessment of crack initiation in the present mechanical analysis. The simulation results are analyzed sequentially for each case, as detailed below:

- *Horizontal configuration:* In this case, increasing the interfacial mobility ratio leads to progressively shallower corrosion pits. When all metal–brine interfaces exhibit equal kinetics ($\bar{M}_\mathrm{R} = 1$), corrosion penetrates more deeply into the ferrite phase, resulting in pits with high depth-to-width ratios (see, Fig. 11a for $\bar{M}_\mathrm{R} = 1$). These geometries promote intense local stress concentrations, making the material more susceptible to early crack initiation. As $\bar{M}_\mathrm{R}$ increases, representing preferential and de-accelerated corrosion of the non-ferrite relative to the ferrite phase, the pit growth in the depth direction is significantly constrained, as depicted in Fig. 11a for cases with $\bar{M}_\mathrm{R} > 1$. This reduction of pit depth with increasing $\bar{M}_\mathrm{R}$ is also reflected in the plot in Fig. 11e. The corroded pit expands laterally within the ferrite phase owing to its relatively higher corrosion kinetics. Due to this, the surface-area-to-volume ratio increases with increasing value of $\bar{M}_\mathrm{R}$, as shown in Fig. 11g. This morphological behavior is consistent with the phase field simulations reported by Zhi et al. [35] and experimental findings of Shih et al. [50]. With increasing $\bar{M}_\mathrm{R}$, broader and flatter pit morphologies develop, which distribute stress more uniformly and reduce peak stress concentrations near the pit base. Consequently, the critical pressure required to initiate a crack increases at $\bar{M}_\mathrm{R} = 2$, when compared with the isotropic kinetics ($\bar{M}_\mathrm{R} = 1$), as shown in Fig. 11f. As for higher values ($\bar{M}_\mathrm{R} = 4, 8$), the pit morphology exhibit high curvature regions, as illustrated in Fig. 11a, that serve as stress concentration sites, resulting in the observed decreasing pattern in the critical pressure for increasing values of $\bar{M}_\mathrm{R} > 1$.
- *Vertical configuration:* For this case, the patterns of corrosion pits are reversed in comparison to the horizontal case (see, Fig. 11b). As the mobility ratio $\bar{M}_\mathrm{R}$ increases, corrosion becomes increasingly localized along the vertically aligned ferrite phase and penetrates deeper into the material, with relatively limited

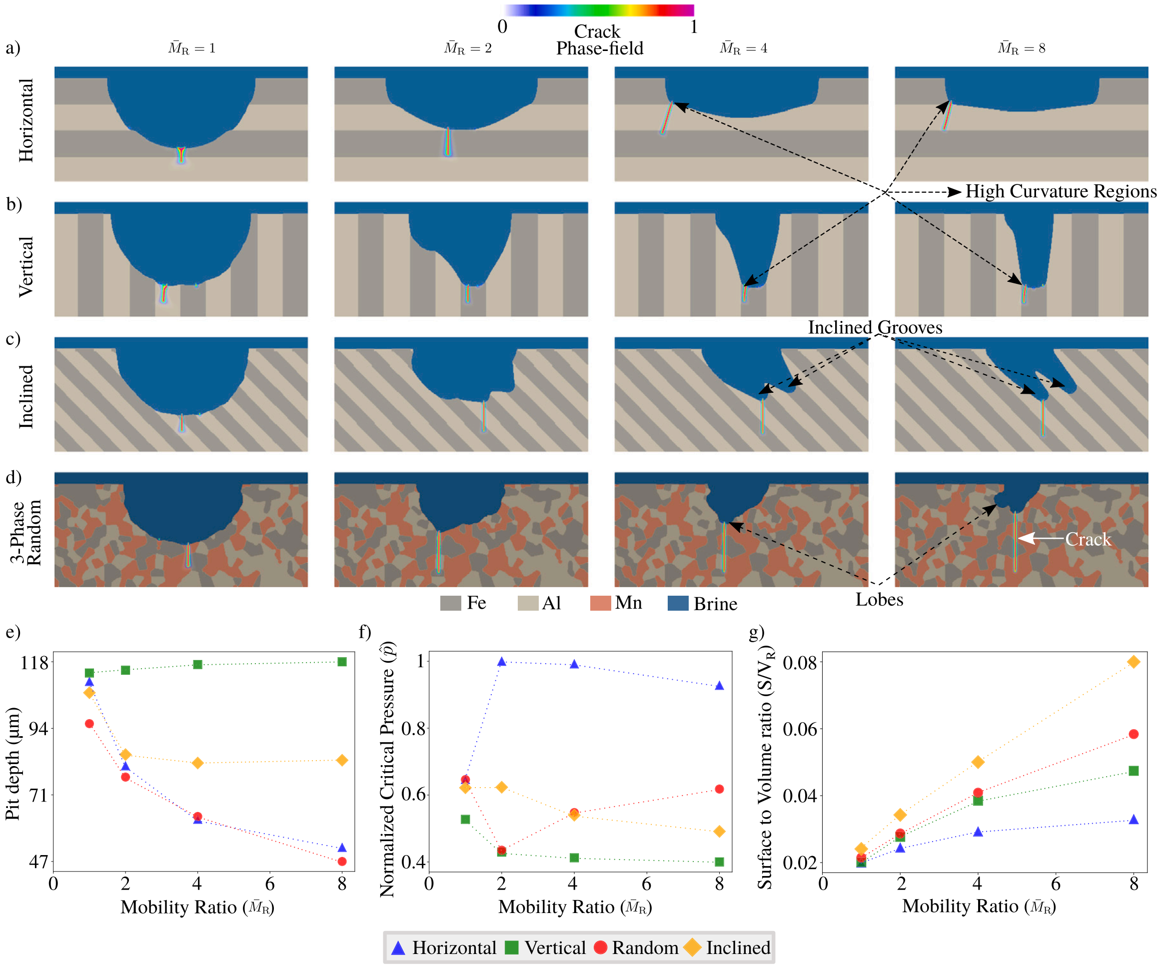

Fig. 11. Pressure-induced cracking in (a) horizontal, (b) vertical, (c) incline and (d) 3-phase polycrystalline system with varying interface mobility ratio $\bar{M}_R$ of the metal–brine interface for the ferrite phase relative to the other metallic phases ($\bar{M}_R = 1, 2, 4, 8$) at $t_{\text{sim}} = 3.5 \times 10^5$, showcasing crack growth. The graphs illustrate the relationship between (e) pit depth, (f) normalized critical pressure, and (g) surface-to-volume ratio with respect to mobility ratio for each of the different phase-orientation cases. For the normalized-pressure comparison in panel f, the normalization uses $p_{\text{crit,max}} = 1265$ MPa for the comparison set shown.

lateral expansion where non-ferrite phase is present. Similar pitting patterns have also been reported in the simulations of Zhi et al. [35] for vertically layered phases. The pit depth increases slightly with increasing $\bar{M}_R$ (see, Fig. 11e), while the surface-to-volume ratio rises more steeply with $\bar{M}_R$ (see, Fig. 11g) due to the narrowing of pits. These narrower pits exhibit higher curvatures near the pit base, which act as stress concentration sites, thereby lowering the critical pressure as $\bar{M}_R$ increases (see, Fig. 11f).

- *Inclined configuration:* In this configuration, the corrosion pitting pattern displays an intermediate behavior between the horizontal and vertical cases. As the mobility ratio increases, the corrosion is pronounced more along the inclined layers of ferrite phases thereby exhibiting narrow groove-like features along the inclined phase boundaries with higher curvature regions (see, Fig. 11c). The presence of corrosion-resistant non-ferrite inclined layers suppresses pitting in these regions as $\bar{M}_R$ increases. This trend is evident in the pit depth versus $\bar{M}_R$ plot in Fig. 11e, which shows a noticeable drop in pit depth for $\bar{M}_R = 2$ compared to $\bar{M}_R = 1$, with pit depth remaining low for $\bar{M}_R = 4$ and $\bar{M}_R = 8$. With increasing $\bar{M}_R$, the narrowing of grooves in the ferrite phases leads to an increase in the surface-area-to-volume ratio S/V_R, as shown in Fig. 11g. Notably, this increase is steepest for the inclined case, owing to the formation of multiple narrow grooves with relatively small volumes. Notably, the critical pressure is similar for mobility ratios $\bar{M}_R = 1$ and 2 (see, Fig. 11f). This can be understood by examining the corresponding pit depths and morphologies. As discussed earlier, the critical pressure decreases with increasing pit depth and with higher curvature in the pit morphology. For $\bar{M}_R = 1$, the pit depth is greater than for $\bar{M}_R = 2$; however, the latter exhibits more pronounced high-curvature regions, which also reduce the critical pressure. The opposing effects of these two morphological factors result in comparable critical pressures for these cases. At higher mobility ratios ($\bar{M}_R = 4, 8$), the pit depth does not decrease substantially, but the extent of high-curvature regions increases, leading to a further reduction in critical pressure (see, Fig. 11f).
- *Polycrystalline configuration:* Fig. 11d shows the simulated pit morphologies for different mobility ratios, $\bar{M}_R$. For $\bar{M}_R = 1$, pit growth is more pronounced than for higher values of $\bar{M}_R > 1$, owing to the random distribution of two corrosion-resistant non-ferrite phases (Al, Mn) and one ferrite phase (Fe) within the polycrystalline microstructure. Increasing $\bar{M}_R$ suppresses pitting, leading to a reduction in pit depth, as also reflected in Fig. 11e.

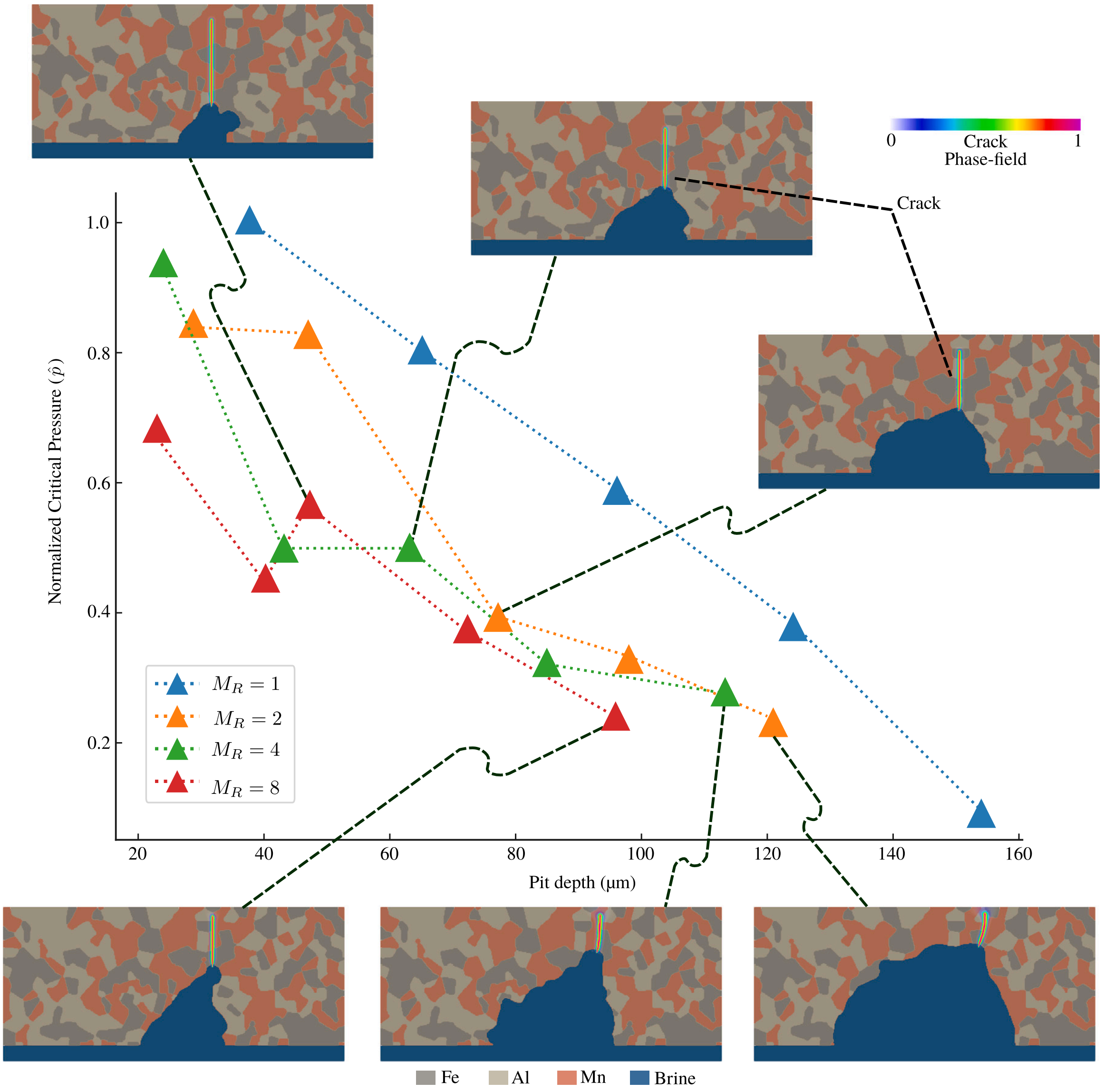

Fig. 12. Normalized critical pressure ($\hat{p}$) as a function of pit depth (in μm) for mobility ratios $\bar{M}_R = 1$, 2, 4, and 8. The upper panel shows representative simulation snapshots of pressure-induced crack evolution at intermediate stages for $\bar{M}_R = 2$, 4, and 8, while the lower panel presents the corresponding later-stage crack propagation for the same mobility ratios. Pressure values were normalized with respect to the critical pressure, $p_{\mathrm{crit,max}} = 1374$ MPa.

With greater mismatch in corrosion kinetics (larger $\bar{M}_R$), the random phase arrangement promotes the development of lobe-like patterns, as seen for $\bar{M}_R = 4$ and 8 in Fig. 11d. The combination of suppressed pit growth and the presence of lobes increases the surface-area-to-volume ratio (S/V_R) with increasing $\bar{M}_R$ (Fig. 11g). Interestingly, the critical pressure exhibits a non-monotonic dependence on $\bar{M}_R$. It decreases from $\bar{M}_R = 1$ to $\bar{M}_R = 2$, despite the latter having a lower pit depth. This reduction is attributed to the emergence of more prominent high-curvature regions in the $\bar{M}_R = 2$ case, which promote crack initiation at a lower critical pressure. This highlights the competing influence of pit depth and curvature on failure resistance. For higher mobility ratios ($\bar{M}_R = 4, 8$), the lobes become smoother with lower curvature, and the pit depth is further reduced, resulting in an increase in critical pressure compared to $\bar{M}_R = 2$.

Given the inherently polycrystalline nature of these alloys, the effect of $\bar{M}_R$ on the corrosion-fracture response was further examined in detail. Fig. 12 presents the normalized critical pressure ($\hat{p}$) required for crack growth as a function of pit depth (μm). For $\bar{M}_R = 1$, the relationship is nearly linear (as discussed in Section 3.2.2), whereas higher $\bar{M}_R$ values introduce pronounced non-linearity and non-monotonicity. This arises because, at larger mobility ratios, pit morphology, particularly the formation of lobes and notch-like features, exerts a stronger influence on failure than pit depth alone. These irregularities generate additional stress concentration sites, which generally lead to lower critical pressures at a given pit depth when $\bar{M}_R > 1$. The random spatial distribution of metallic phases with different corrosion resistances (Al, Mn, Fe) further enhances these irregularities, thereby amplifying the non-monotonic behavior observed in the critical pressure vs. pit depth plots. Simulation snapshots for $\bar{M}_R = 2$, 4, and 8 at intermediate and later stages (Fig. 12) reveal the irregular and complex progression of the pit front, resulting in the formation of multiple localized high-stress regions.

Overall, the results demonstrate that in the polycrystalline system, increasing $\bar{M}_R$ tends to suppress pit growth, however, the accompanying changes in pit morphology, particularly the formation of lobes and notch-like features, can outweigh the effect of reduced pit depth and exert a dominant influence on crack growth and the critical pressure required for failure.

Key insights. This study demonstrates that the interfacial mobility mismatch has a pronounced, configuration-dependent influence on both pit morphology and failure susceptibility. Importantly, the role of kinetic mismatch extends well beyond its impact on pit depth.

- *Failure risk is not solely depth-driven, but also shape-modulated*: The simulations reveal that pit depth alone does not fully capture the failure risk, the pit's morphology, particularly the presence of high-curvature features such as lobes, grooves, and notches, plays a decisive role. While deeper pits reduce cross-sectional load-bearing capacity, high-curvature regions act as local stress concentrators, accelerating crack initiation and propagation. Increasing the mismatch between the corrosion kinetics of different metallic phases raises the surface-area-to-volume ratio irrespective of phase configurations, primarily through the development of these high-curvature features. The magnitude of this effect, however, is sensitive to the phase arrangement. The critical pressure is dictated by the interplay between pit depth (global weakening) and morphological sharpness (local stress concentration), and this interplay can lead to non-monotonic relations between critical pressure and mobility mismatch.
- *Implications for designing corrosion-resistant alloys*: The results suggest that careful selection of alloy chemistry and phase configuration can be used to tune corrosion behavior and mitigate failure risk. In particular, engineering microstructures to limit high-curvature pit features, through phase boundary alignment, phase connectivity control, or controlling metal-brine kinetics, could substantially enhance damage tolerance. The findings underscore the importance of designing alloys not only for uniform corrosion resistance but also for morphology-controlled pitting, thereby reducing stress concentration effects that drive mechanical failure.

Taken together, these insights provide practical guidance for alloy and microstructure design in corrosion-prone environments. Rather than focusing exclusively on reducing average corrosion rates, the results indicate that mitigating localized kinetic mismatch and suppressing the formation of sharp pit features can substantially improve resistance to corrosion-assisted cracking. From a design perspective, this suggests prioritizing phase combinations and interface energetics that promote smoother dissolution fronts, as well as tailoring phase connectivity to limit stress amplification at pit bases. While the present framework does not prescribe specific alloy compositions, it establishes mechanistic criteria that can inform microstructure-aware strategies for designing alloys with enhanced tolerance to localized corrosion and pressure-induced failure.

4. Conclusion and outlook

This work presents a grand-potential phase-field framework for simulating dissolution-driven pit evolution in multiphase alloys together with a diffuse-interface formulation for pressure-induced crack initiation. By treating corrosion and fracture sequentially, the approach captures how evolving pit morphology governs the mechanical integrity of metallic components exposed to aggressive environments. Validation against analytical benchmarks and established numerical tests demonstrates quantitative agreement for both dissolution kinetics and the diffuse application of mechanical loads, providing a robust basis for mesoscale simulations. Across all microstructures considered, pit depth and local geometric curvature emerge as the dominant factors controlling the reduction in critical pressure for crack initiation. While single-phase alloys exhibit largely depth-driven behavior, dual-phase and polycrystalline systems develop persistent high-curvature features that promote early failure. Variations in interfacial mobility introduce additional morphological irregularity, leading to non-monotonic failure trends and highlighting the strong sensitivity of corrosion-assisted cracking to kinetic mismatch. These results clarify how microstructural topology, phase arrangement, and dissolution kinetics jointly influence the transition from localized material loss to pressure-induced fracture. The modeling framework is subject to several simplifying assumptions that define its scope. Accelerated diffusion coefficients are used to reduce computational cost, affecting absolute timescales but not the underlying mechanistic trends. The simulations are restricted to two-dimensional geometries, employ linear elastic material behavior with homogeneous fracture resistance, and treat corrosion and fracture sequentially rather than within a fully coupled chemo-mechanical formulation. Accordingly, the present fracture formulation should be interpreted as a brittle fracture mesoscale model for morphology-driven crack initiation under pressure loading. It does not capture yielding, plastic blunting, ductile tearing, or other inelastic fracture mechanisms that may become important in real multiphase alloys. As a result, the present framework is intended as a mechanistic mesoscale model for morphology-to-failure transitions rather than as a fully coupled quantitative predictive tool. In regimes where local tensile stress significantly alters dissolution kinetics, destabilizes passivation, or promotes stress-assisted corrosion, the present sequential treatment may overestimate the resistance to failure. Accordingly, the absolute critical pressure thresholds reported in this work should be interpreted as model-scale comparative quantities rather than as material-calibrated engineering failure predictions.

In addition, the alloy microstructures considered are idealized rather than experimentally reconstructed. Moreover, the diffuse-interface length scales were kept fixed relative to the mesh, so the reported fracture pressures should be interpreted as comparative trends at fixed regularization rather than as mesh-converged material-specific values. These limitations do not alter the mechanistic conclusions of this study but provide clear directions for future refinement. Fully coupled chemo-mechanical interactions therefore remain an important direction for future model development.

The versatility of the framework enables its extension to three-dimensional microstructures, experimentally calibrated dissolution kinetics, and fully coupled chemo-mechanical interactions relevant to geothermal, nuclear, and chemical processing environments. An important next step is the extension of the present framework to fully three-dimensional, experimentally reconstructed microstructures and component-relevant geometries, which would enable more realistic assessment of pit curvature evolution, crack-front development, and microstructure-sensitive failure thresholds. A key next step towards engineering application is the calibration of interfacial mobility parameters against experimentally accessible observables such as pit depth versus time, preferential phase dissolution, and electrochemical response under controlled brine chemistry and temperature conditions. An important next step is a more detailed quantitative analysis of post-initiation crack evolution, including crack length and propagation kinetics under different pit morphologies and loading paths. This would, however, require extending the present quasi-static fracture formulation to a dynamic fracture-mechanics framework in which crack growth can be described on a physically meaningful timescale. Complementing this, the incorporation of elastic–plastic or ductile phase-field fracture formulations would enable more realistic quantitative prediction in alloys where plastic deformation significantly influences crack initiation and growth. In particular, the results suggest that controlling phase connectivity, interfacial mobility contrasts, and pit surface curvature through alloy design and microstructural engineering offers a viable pathway to mitigate corrosion-induced failure. Future efforts will focus on incorporating realistic brine chemistries, phase-specific elastic heterogeneity, phase-specific fracture resistance and interfacial decohesion behavior, as well as long-term pit evolution in three dimensions, to support predictive lifetime assessment and microstructure-informed alloy design. The methodology established here provides a foundation for integrating corrosion modeling with structural reliability assessments in environments where localized dissolution and fluid pressure coexist.

CRediT authorship contribution statement

Akash Kumar: Conceptualization, Methodology,Software, Validation,Formal analysis,Investigation, Visualization, Writing – original draft,Writing – review & editing. **Nishant Prajapati:** Conceptualization,Methodology,Supervision,Writing – review & editing. **Martin Reder:** Methodology,Software,Supervision,Writing – review & editing. **Ravi Kumar Jeela:** Methodology, Software,Writing – review & editing. **Daniel Schneider:** Conceptualization:Supervision, Writing – review & editing. **Britta Nestler:** Supervision, Funding Acquisition, Resources,Writing – review & editing.

Declaration of Generative AI and AI-assisted technologies in the writing process

During the preparation of this work, the authors used generative AI tools (ChatGPT by OpenAI) to assist with language refinement, grammar corrections, and improvement of sentence clarity. After using this tool, the authors reviewed and edited the content as needed and take full responsibility for the content of the publication.

Funding information

We thank the Helmholtz association for funding the main parts of the modeling and simulation research work under the program “MTET: 38.04.04”.

Declaration of competing interest

The authors declare that they have no known competing financial interests or personal relationships that could have appeared to influence the work reported in this paper.

Acknowledgments

The authors acknowledge support by the state of Baden-Württemberg through bwHPC and also thank Mr. Muhammad Umar from the University of Applied Science, Karlsruhe for the engaging discussions on the topic.

Appendix A. Analytical solution for the bending beam benchmark

To validate the diffuse application of the stress boundary condition, we consider an Euler–Bernoulli bending beam of length L, height H, and depth B, with $L \gg H$. Under the assumptions of geometrical linearization and vanishing Poisson ratio $\nu = 0$, the normal stress component σ_{11} in the beam satisfies

$$\sigma_{11} = -Ez\frac{\mathrm{d}^2 w}{\mathrm{d}x^2} = E\varepsilon_{11}, \tag{A.1}$$

where $w(x)$ is the transverse displacement, ε_{11} the corresponding strain, E the Young’s modulus, and z the vertical coordinate measured from the neutral axis. If the beam is loaded with a spatially constant pressure p on the top surface, this is equivalent to a line force density $q := pB$. Using the geometrical moment of inertia

$$I_y = \int_A z^2 \,\mathrm{d}A = \frac{BH^3}{12}, \tag{A.2}$$

with A the cross-section of the beam, and defining the bending moment (torque)

$$M_y(x) = \int_A z\,\sigma_{11}(x,z)\,\mathrm{d}A, \tag{A.3}$$

the analytical solution for the clamped–free beam can be written as

$$w(x) = \frac{qL^4}{8EI_y}\,\frac{1}{3}\left[\left(\frac{x}{L}\right)^4 - 4\left(\frac{x}{L}\right)^3 + 6\left(\frac{x}{L}\right)^2\right] =: \frac{qL^4}{8EI_y}\,\tilde{w}(x), \tag{A.4a}$$

$$M_y(x) = \frac{qL^2}{2}\left[-\left(\frac{x}{L}\right)^2 + 2\frac{x}{L} - 1\right] =: \frac{qL^2}{2}\,\tilde{M}(x), \tag{A.4b}$$

$$\sigma_{11}(x,z) = \frac{M_y(x)}{I_y}\,z. \tag{A.4c}$$

The normalized quantities used in the main text are defined as

$$\tilde{x} := \frac{x}{L}, \qquad \tilde{w} := \frac{w}{\max(w)}, \qquad \tilde{M} := \frac{M_y}{\max(|M_y|)}, \tag{A.5}$$

with $\max(w) = qL^4/(8EI_y)$ and $\max(|M_y|) = qL^2/2$.

Appendix B. Richardson extrapolation procedure

To quantify the convergence behavior of the diffuse-interface formulation, Richardson extrapolation (RE) is employed. Consider a solution quantity Ψ that depends on the discretization step size h, with an asymptotic error expansion

$$\Psi(h) = \Psi(h=0) + ah^m + \mathcal{O}(h^{m+1}), \tag{B.1}$$

where $\Psi(h=0)$ is the (unknown) exact solution, a is a constant, and m is the order of accuracy determined by the numerical scheme. The quantity Ψ may be a field variable or an integral quantity derived from the solution of a PDE system. Neglecting higher-order terms, approximations $\hat{\Psi}$ and $\hat{m}$ of the exact solution and order of accuracy can be obtained using numerical solutions $\Psi_i := \Psi(h_i)$ on three successively refined grids with $h_1 < h_2 < h_3$. Writing

$$\hat{\Psi} = \Psi_i + \hat{a}h_i^{\hat{m}}, \quad i = 1,2,3, \tag{B.2}$$

and following the approach of Celik et al. [47] to account for possible oscillatory convergence, we define

$$r_{21} := \frac{h_2}{h_1}, \qquad r_{32} := \frac{h_3}{h_2}, \qquad \theta := \frac{r_{32}}{r_{21}}\,\frac{\Psi_2 - \Psi_1}{\Psi_3 - \Psi_2}. \tag{B.3}$$

Then,

$$\hat{m} = \frac{1}{\ln(r_{21})}\left|\ln\left|\frac{\Psi_3 - \Psi_2}{\Psi_2 - \Psi_1}\right| + \left(\frac{r_{21}^{\hat{m}} - \operatorname{sign}(\theta)}{r_{32}^{\hat{m}} - \operatorname{sign}(\theta)}\right)\right|, \tag{B.4a}$$

$$\hat{\Psi} = \Psi_1 + \frac{\Psi_1 - \Psi_2}{r_{21}^{\hat{m}} - 1}, \tag{B.4b}$$

$$\hat{a} = \frac{1}{h_1^{\hat{m}}}\,\frac{\Psi_1 - \Psi_2}{r_{21}^{\hat{m}} - 1}, \tag{B.4c}$$

where $\operatorname{sign}(\cdot)$ denotes the signum function. For the special case $r_{21} = r_{32}$, Eq. (B.4) can be solved directly; otherwise, a numerical root-finding procedure (e.g. Newton’s method) is used to determine $\hat{m}$. In the case of field quantities, we follow Cadafalch et al. [48] and interpolate the solutions on each grid onto the coarsest grid (with step size h_3) using third-order spline interpolation, ensuring that interpolation errors remain negligible compared to discretization errors. The averaged order of accuracy over all grid points is then used in the RE expressions above. This procedure is applied to the normalized displacement $\tilde{w}$ and torque $\tilde{M}$ in the beam benchmark to obtain the extrapolated solutions reported in Table 2.

Appendix C. Diffuse-interface estimate of the geometric moment of inertia

In the diffuse-interface setting, the geometrical moment of inertia of the beam is computed as

$$I_y^{\mathrm{d}} = \int_V \phi(z)\,z^2\,\mathrm{d}A, \tag{C.1}$$

where $\phi(z)$ is the phase-field variable distinguishing solid ($\phi \approx 1$) from void or fluid ($\phi \approx 0$), V denotes the extended domain containing the beam and diffuse interface, and z is measured from the beam mid-plane. Due to the nonlinearity of the factor z^2 in the integrand, values of ϕ at $|z| > H/2$ (within the diffuse interface) are weighted more strongly than those at $|z| < H/2$. This leads to a slight overestimation of the effective moment of inertia compared to the sharp-interface value. For the obstacle potential used in this work, the one-dimensional equilibrium phase-field profile in the interface normal coordinate η is given by

$$\phi(\eta) = \frac{1}{2}\left[1 - \sin\left(\frac{\pi\eta}{\delta}\right)\right], \tag{C.2}$$

where $\eta := z \pm H/2$ at the upper and lower sides of the beam, respectively, and δ denotes the diffuse-interface thickness. Using this profile, the diffuse-interface moment of inertia can be evaluated analytically as

$$\begin{aligned} I_y^{\mathrm{d}}(\delta) &= \frac{BH^3}{12}\left[1 + 3\left(\frac{\delta}{H}\right)^2\left(1 - \frac{8}{\pi^2}\right)\right] \\ &\approx \frac{BH^3}{12}\left[1 + 0.5683\left(\frac{\delta}{H}\right)^2\right]. \end{aligned} \tag{C.3}$$

Thus, $I_y^{\mathrm{d}} > I_y$ for finite δ, and the relative overestimation scales with $(\delta/H)^2$. This explains why, at coarse resolution (large δ/H), the displacement field exhibits larger numerical errors than the torque, which depends more directly on the stress distribution. In the sharp-interface limit $\delta \to 0$, the diffuse-interface value I_y^{d} converges to the classical result $BH^3/12$, and the associated model error vanishes.

Data availability

The simulation data supporting the findings of this study are publicly available in the open-access Zenodo repository [51], including processed simulation output files (`.vtk`) and representative input files (`.infile`) required to reproduce the results shown in Figures 1, 2, 5, and 8–12. Figures 3, 4, 6, and 7 are schematic illustrations or derived plots and therefore do not have associated raw simulation datasets.

All simulations were performed using the PACE3D phase-field framework, which is licensed software. While the solver itself is not publicly distributed, the provided input files and datasets enable reproduction of the published results by users with access to the PACE3D framework. Visualization of the simulation output files can be performed using standard tools such as ParaView.

References

[1] Szklarska-Smialowska Z. Review of literature on pitting corrosion published since 1960. Corrosion 1971;27(6):223–33.

[2] Frankel G. Pitting corrosion of metals a review of the critical factors. J Electrochem Soc 1998;145(6):2186–98.

[3] Dolley E, Lee B, Wei R. The effect of pitting corrosion on fatigue life. Fatigue Fract Eng Mater Struct 2000;23(7):555–60.

[4] Sedriks A. Corrosion of stainless steel. John Wiley and Sons, Inc; 1996.

[5] Sankaran K, Perez R, Jata K. Effects of pitting corrosion on the fatigue behavior of aluminum alloy 7075-T6: modeling and experimental studies. Mater Sci Eng: A 2001;297(1):223–9.

[6] Penot C, Martelo D, Paul S. Corrosion and scaling in geothermal heat exchangers. Appl Sci 2023;13(20):11549.

[7] Yang J, Li C, Pan Y, Huang H. The failure mechanism of the 316 SS heat exchanger tube in the geothermal water environment. Materials 2022;15(22):8103.

[8] Shannon D. Economic impact of corrosion and scaling problems in geothermal energy systems. Tech. rep., Richland, Wash.(US): Battelle Pacific Northwest Labs; 1975.

[9] Scully JC. Fundamentals of corrosion. Elmsford, NY: Pergamon Press Inc.; 1974.

[10] Nogara J, Zarrouk SJ. Corrosion in geothermal environment Part 2: Metals and alloys. Renew Sustain Energy Rev 2018;82:1347–63.

[11] Poulain M, Dupin J-C, Tillous KE, Ledeuil J-B, Serin J-P, Cézac P, Martinez H. Surface analyses of low carbon steel and stainless steel in geothermal synthetic Na-Ca-Cl brine saturated with CO2. Results Surf Interfaces 2022;7:100040.

[12] Liu S, Yue C, Chen X, Zhu Q, Tu Y. Pitting corrosion resistance on annealing treated super duplex stainless steel S32750. Crystals 2020;10(4):294.

[13] Thomas R. Titanium in the geothermal industry. Geothermics 2003;32(4–6):679–87.

[14] Liu M, Du C, Liu Z, Wang L, Zhong R, Cheng X, Ao J, Duan T, Zhu Y, Li X. A review on pitting corrosion and environmentally assisted cracking on duplex stainless steel. Microstructures 2023;3.

[15] Ateya B, Pickering H. Effects of ionic migration on the concentrations and mass transfer rate in the diffusion layer of dissolving metals. J Appl Electrochem 1981;11(4):453–61.

[16] Tester T, Isaacs H. Diffusional effects in simulated localized corrosion. J Electrochem Soc 1975;122(11):1438–45.

[17] Turnbull A, Thomas J. A model of crack electrochemistry for steels in the active state based on mass transport by diffusion and ion migration. J Electrochem Soc 1982;129(7):1412–22.

[18] Sharland S, Jackson C, Diver A. A finite element model of the propagation of corrosion crevices and pits. Corros Sci 1989;29(9):1149–66.

[19] Xiao J, Chaudhuri S. Predictive modeling of localized corrosion: an application to aluminum alloys. Electrochim Acta 2011;56(16):5630–41.

[20] Kota N, Qidwai S, Lewis A, DeGiorgi V. Microstructure-based numerical modeling of pitting corrosion in 316 stainless steel. ECS Trans 2013;50(31):155–64.

[21] Sethian J. A fast marching level set method for monotonically advancing fronts. Proc Natl Acad Sci USA 1996;93(4):1591–5.

[22] Sharland S. A review of the theoretical modelling of crevice and pitting corrosion. Corros Sci 1987;27(3):289–323.

[23] Sarkar S, Warner J, Aquino W. A numerical framework for the modeling of corrosive dissolution. Corros Sci 2012;65:502–11.

[24] Jafarzadeh S, Chen Z, Bobaru F. Computational modeling of pitting corrosion. Corros Rev 2019;37(5):419–39.

[25] Malki B, Baroux B. Computer simulation of the corrosion pit growth. Corros Sci 2005;47(1):171–82.

[26] Guyer JE, Boettinger WJ, Warren JA, McFadden GB. Phase-field modeling of electrochemistry. I. Equilibrium. Phys Rev E 2004;69(2):021603.

[27] Mai W, Soghrati S, Buchheit RG. A phase field model for simulating the pitting corrosion. Corros Sci 2016;110:157–66.

[28] Tsuyuki C, Yamanaka A, Ogimoto Y. Phase-field modeling for pH-dependent general and pitting corrosion of iron. Sci Rep 2018;8(1):12777.

[29] Ansari TQ, Xiao Z, Hu S, Li Y, Luo J-L, Shi S-Q. Phase-field model of pitting corrosion kinetics in metallic materials. Npj Comput Mater 2018;4(1):38.

[30] Mai W, Soghrati S. A phase field model for simulating the stress corrosion cracking initiated from pits. Corros Sci 2017;125:87–98.

[31] Lin C, Ruan H. Phase-field modeling of mechano–chemical-coupled stress-corrosion cracking. Electrochim Acta 2021;395:139196.

[32] Cui C, Ma R, Martínez-Pañeda E. A generalised, multi-phase-field theory for dissolution-driven stress corrosion cracking and hydrogen embrittlement. J Mech Phys Solids 2022;166:104951.

[33] Choudhury A, Nestler B. Grand-potential formulation for multicomponent phase transformations combined with thin-interface asymptotics of the double-obstacle potential. Phys Rev E 2012;85(2):021602.

[34] Hötzer J, Reiter A, Hierl H, Steinmetz P, Selzer M, Nestler B. The parallel multi-physics phase-field framework Pace3D. J Comput Sci 2018;26:1–12.

[35] Zhi H, Dong P, Li K, Gao L, Zhou W, Zhang H. Phase field study of pitting corrosion: Electrochemical reactions and temperature dependence. Comput Mater Sci 2024;244:113251.

[36] Hötzer J, Tschukin O, Said MB, Berghoff M, Jainta M, Barthelemy G, Smorchkov N, Schneider D, Selzer M, Nestler B. Calibration of a multi-phase field model with quantitative angle measurement. J Mater Sci 2016;51(4):1788–97.

[37] Hoffrogge PW, Mukherjee A, Nani E, Amos PK, Wang F, Schneider D, Nestler B. Multiphase-field model for surface diffusion and attachment kinetics in the grand-potential framework. Phys Rev E 2021;103(3):033307.

[38] Li X, Lowengrub J, Rätz A, Voigt A. Solving PDEs in complex geometries: a diffuse domain approach. Commun Math Sci 2009;7(1):81–107.

[39] Reder M, Holland-Cunz J, Lorson P, August A, Nestler B. Simulative determination of effective mechanical properties for digitally generated foam geometries. Adv Eng Mater 2023;25(19):2300340.

[40] Miehe C, Welschinger F, Hofacker M. Thermodynamically consistent phase-field models of fracture: Variational principles and multi-field FE implementations. Internat J Numer Methods Engrg 2010;83(10):1273–311.

[41] Yoigt W. Uber die beziehungzwischen den beiden elastizitats konstanten isotroper korper. Wied Ann 1889;38:573–87.

[42] Schöller L, Schneider D, Herrmann C, Prahs A, Nestler B. Phase-field modeling of crack propagation in heterogeneous materials with multiple crack order parameters. Comput Methods Appl Mech Engrg 2022;395:114965.

[43] Scheiner S, Hellmich C. Stable pitting corrosion of stainless steel as diffusion-controlled dissolution process with a sharp moving electrode boundary. Corros Sci 2007;49(2):319–46.

[44] Ernst P, Newman R. Pit growth studies in stainless steel foils. I. Introduction and pit growth kinetics. Corros Sci 2002;44(5):927–41.

[45] Ernst P, Newman R. Pit growth studies in stainless steel foils. II. Effect of temperature, chloride concentration and sulphate addition. Corros Sci 2002;44(5):943–54.

[46] Scheiner S, Hellmich C. Stable pitting corrosion of stainless steel as diffusion-controlled dissolution process with a sharp moving electrode boundary. Corros Sci 2007;49(2):319–46.

[47] Celik I, Ghia U, Roache P, Freitas C, Coleman H, Raad P, Celik Ì, Freitas C, Coleman H. Procedure for estimation and reporting of uncertainty due to discretization in CFD applications. J Fluids Eng 2008;130(7).

[48] Cadafalch J, Pérez-Segarra C, Consul R, Oliva A. Verification of finite volume computations on steady-state fluid flow and heat transfer. J Fluids Eng 2002;124(1):11–21.

[49] Schneider D, Schoof E, Tschukin O, Reiter A, Herrmann C, Schwab F, Selzer M, Nestler B. Small strain multiphase-field model accounting for configurational forces and mechanical jump conditions. Comput Mech 2018;61(3):277–95.

[50] Shih S, Tai C, Perng T. Corrosion behavior of two-phase fe-mn-al alloys in 3.5% NaCl solution. Corrosion 1993;49(2):130–4.

[51] Kumar A, Prajapati N, Reder M, Jeela RK, Schneider D, Nestler B. Dataset for modeling pitting corrosion and Pressure-driven cracking in multiphase alloys. 2026, http://dx.doi.org/10.5281/zenodo.18182609.